Published in final edited form as:
Nature. 2018 February 01; 554(7690): 62–68. doi:10.1038/nature25459.

Evolutionary routes and *KRAS* dosage define pancreatic cancer phenotypes

Sebastian Mueller[1,2,*], Thomas Engleitner[1,2,3,*], Roman Maresch[1,2,3,*], Magdalena Zukowska[1,2], Sebastian Lange[1,2], Thorsten Kaltenbacher[1,2,3], Björn Konukiewitz[4], Rupert Öllinger[1,2], Maximilian Zwiebel[2], Alex Strong[5], Hsi-Yu Yen[3,6], Ruby Banerjee[5], Sandra Louzada[5], Beiyuan Fu[5], Barbara Seidler[1,2], Juliana Götzfried[2], Kathleen Schuck[2], Zonera Hassan[2], Andreas Arbeiter[2], Nina Schönhuber[1,2], Sabine Klein[1,2], Christian Veltkamp[1,2], Mathias Friedrich[5], Lena Rad[2], Maxim Barenboim[2,3], Christoph Ziegenhain[7], Julia Hess[8], Oliver M. Dovey[5], Stefan Eser[2], Swati Parekh[7], Fernando Constantino-Casas[9], Jorge de la Rosa[5,10,11], Marta I. Sierra[12], Mario Fraga[12,13], Julia Mayerle[14], Günter Klöppel[4], Juan Cadiñanos[5,10], Pentao Liu[5], George Vassiliou[5], Wilko Weichert[3,4], Katja Steiger[4,6], Wolfgang Enard[7], Roland M. Schmid[2,3], Fengtang Yang[5], Kristian Unger[8], Günter Schneider[2,3], Ignacio Varela[15], Allan Bradley[5], Dieter Saur[1,2,3,#], and Roland Rad[1,2,3,#,§]

[1]Center for Translational Cancer Research (TranslaTUM), Technische Universität München, Munich, Germany

[2]Department of Medicine II, Klinikum rechts der Isar, Technische Universität München, Munich, Germany

[3]German Cancer Consortium (DKTK), German Cancer Research Center (DKFZ), Heidelberg, Germany

[4]Institute of Pathology, Technische Universität München, Munich, Germany

[5]The Wellcome Trust Sanger Institute, Genome Campus, Hinxton/Cambridge, UK

[6]Comparative Experimental Pathology, Technische Universität München, Munich, Germany

[§]Correspondence and requests for materials should be addressed to R. R. (roland.rad@tum.de).
[*]These authors contributed equally to this work.
[#]These authors jointly supervised this work.

Author Contributions

S.M., D.S., R.R. designed the study; S.M., T.E., R.M., D.S., R.R. interpreted and visualized data; T.E., S.La., M.Zw., M.B. conducted bioinformatic analyses. S.M., T.E., R.M., S.La., M.Zw., I.V. developed bioinformatic analyses strategies; S.M., R.M., M.Zu., T.K., A.S., B.S., J.G., K.Sc., Z.H., A.A., N.S., C.V. L.R. isolated mPDAC cell cultures; S.M., R.M., J.H., K.U. performed genomics with help from R.Ö.; R.Ö., C.Z. conducted RNA-Seq; R.B., S.Lo., B.F., S.K., K. St., F.Y. performed cytogenetics; B.K. performed microdissection; B.K., H-Y.Y., G.K., W.W., K.St. carried out pathological assessment; C.Z., S.P., W.E., K.U., I.V. contributed analytic tools; M.Fri., O.M.D., S.E., F.C-C., J.R., M.I.S., M.Fra., J.M., G.K., R.M.S., J.C., P.L., G.V., W.W., K.St., W.E., G.S., A.B., D.S., R.R. provided resources and critical input; D.S., R.R. supervised the study; S.M., R.R. wrote the manuscript; T.E., R.M. and D.S. edited the manuscript.

Author Information

Reprints and permissions information is available at www.nature.com/reprints. Readers are welcome to comment on the online version of the paper.

The authors declare no competing financial interests.

Europe PMC Funders Author Manuscripts

[7]Anthropology & Human Genomics, Department of Biology II, Ludwig-Maximilians Universität, Martinsried, Germany

[8]Helmholtz Zentrum München, Research Unit Radiation Cytogenetics, Neuherberg, Germany

[9]Department of Veterinary Medicine, University of Cambridge, Cambridge, UK

[10]Instituto de Medicina Oncológicay Molecular de Asturias (IMOMA), Oviedo, Spain

[11]Departamento de Bioquímica y Biología Molecular, Facultad de Medicina, Instituto Universitario de Oncología (IUOPA), Universidad de Oviedo, Oviedo, Spain

[12]Institute of Oncology of Asturias (IUOPA), HUCA, Universidad de Oviedo, Oviedo, Spain

[13]Nanomaterials and Nanotechnology Research Center (CINN-CSIC), Universidad de Oviedo, El Entrego, Spain

[14]Medizinische Klinik und Poliklinik II, Klinikum der LMU München-Grosshadern, Munich, Germany

[15]Instituto de Biomedicina y Biotecnología de Cantabria (UC-CSIC), Santander, Spain

Abstract

The poor correlation of mutational landscapes with phenotypes limits our understanding of pancreatic ductal adenocarcinoma (PDAC) pathogenesis and metastasis. Here we show a critical role of oncogenic dosage-variation in PDAC biology and phenotypic diversification. We found gene-dosage increase of mutant $KRAS^{MUT}$ in human PDAC precursors, driving both early tumorigenesis and metastasis, thus rationalizing early PDAC dissemination. To overcome limitations posed to gene-dosage studies by PDAC´s stroma-richness we developed large cell culture resources of metastatic mouse PDAC. Integration of their genomes, transcriptomes and tumor phenotypes with functional studies and human data, revealed additional widespread effects of oncogenic dosage-variation on cell morphology/plasticity, histopathology and clinical outcome, with highest $Kras^{MUT}$ levels underlying aggressive undifferentiated phenotypes. We also identify alternative oncogenic gains (*Myc, Yap1 or Nfkb2*), which collaborate with heterozygous $Kras^{MUT}$ in driving tumorigenesis, yet with lower metastatic potential. Mechanistically, different oncogenic gains and dosages evolve along distinct evolutionary routes, licensed by defined allelic states and/or combinations of hallmark tumor-suppressor alterations (*Cdkn2a*, *Trp53,* Tgfβ-pathway). Thus, evolutionary constraints and contingencies direct oncogenic dosage gain and variation along defined routes to drive early progression and shape downstream PDAC biology. Our study uncovers universal principles in *Ras*-driven oncogenesis with potential relevance beyond pancreatic cancer.

Pancreatic ductal adenocarcinoma (PDAC) is the fourth leading cause of cancer-related death and is expected to become the second within the next decade1. Whilst treatments constantly improved for many other cancer types, 5-year survival rates in PDAC stayed around 5%1. Genome sequencing revealed extensive genetic heterogeneity beyond a few frequently mutated drivers2–8 like *KRAS*, *TP53*, *CDKN2A* or TGFβ-pathway alterations. Disappointingly however, genomic changes could so far not be broadly linked to biologic, morphologic or clinical phenotypes. In addition, the molecular basis of cancer cell

dissemination is poorly understood, and genetic comparisons of primary/metastasis pairs could not identify recurrent alterations linked to metastasis3,8. Critical limitations to human PDACs (hPDAC) genomics are (i) the cancer genome complexity, posing challenges to their interpretation, (ii) the high (and variable) stromal content, which confounds particularly gene-dosage analyses and transcriptome interpretation, (iii) the limited availability of human cell culture-based resources to overcome this problem and (iv) the scarcity of paired primary/metastasis tissues, particularly of treatment-naive ones, e.g. for evolutionary studies. Here we characterized large murine PDAC cell line resources and combined the results with cross-species comparisons and functional studies to unravel molecular principles underlying PDAC evolution and phenotypic diversification.

Genetic landscapes of mouse PDAC

We initially characterized primary PDAC cell cultures from 38 mice expressing $Kras^{G12D}$ conditionally in the pancreas (PK mice)9,10 by multiplex FISH (M-FISH), whole-exome sequencing (WES) and array comparative genomic hybridization (aCGH). We developed a pipeline for WES data analysis allowing mouse/human comparisons using identical parameter settings. A WES study on microdissected human PDAC (reduced stromal "contamination") served as the reference human data set6. Somatic mutation calling identified 318 synonymous and 606 non-synonymous mutations in 38 mPDACs (Extended Data Fig. 1a and Supplementary Table 1). Mutational patterns were similar, (Fig. 1a; Supplementary Table 2, Extended Data Fig. 1b-g) but mutational burdens were significantly higher in hPDAC than mPDAC, with 3.3 and 1.5 fold increased median SNV and indel numbers, respectively (Fig. 1b and Supplementary Tables 1, 3-5). Recurrently altered genes were infrequent in mice. A subset overlapped with recurrently mutated genes in human cancers and/or common insertion sites in pancreas-specific transposon screens11–13 (Extended Data Fig. 1a).

Structural changes were also less common in mPDAC (Fig. 1b, Supplementary Tables 6-8). There was however substantial variation between cancers, with some mPDACs having only few focal alterations, but others showing extensive changes, including clustered intra-chromosomal alterations, aneuploidy and inter-chromosomal translocations (Fig. 1c and Extended Data Fig. 1h-l). Notably, 34% (14/38) tumors had complex rearrangements, with ten or more alterations per affected chromosome. The majority (12/14) of such events affect chr4, invariably involving *Cdkn2a*. One cancer showed massively rearranged chr15 with high-level *Myc* amplification and another tumor had clustered chr1 rearrangements (Extended Data Fig. 2a-n). These findings reflect selection of complex rearrangements that affect cancer drivers.

The regularity of oscillating copy number states in most cancers suggested chromothripsis as the predominant process underlying these complex alterations. Whole-genome sequencing, followed by rearrangement analysis and computational simulations confirmed all hallmarks defining the one-off nature of chromothripsis14, including clustering of breakpoints, regularity of oscillating copy number states, identical CNA and LOH patterns, randomness of DNA segment order/joints and alternating head-tail sequences (Fig. 1d and detailed

analyses in Extended Data Fig. 2p-y. In addition, M-FISH confirmed chr4 content loss affecting only one haplotype (Fig. 1d).

Complex rearrangements were proposed to trigger accelerated evolution of human PDAC15. The mouse model allows experimental interrogation of this hypothesis due to the "synchronized" nature of tumor initiation ($Kras^{G12D}$-mutation). We found that time-to-tumor development was indeed shorter in animals with *Cdkn2a* loss through catastrophic events (Fig. 1e and Extended Data Fig. 2o). A subset (16%) of complex rearrangements in hPDAC disrupts multiple known tumor suppressors through translocations15. Chromothripsis-associated chr4 translocations were also frequent in mice (Fig. 1c), although no recurrent translocation partners were found.

$Kras^{MUT\text{-}iGD}$ links early progression & metastasis

The most common amplification affected the *Kras* locus (Extended Data Fig. 3a,b), which is also frequent in hPDAC16,17. Combined analyses of M-FISH, aCGH and *Kras* mutant/wild-type (wt) allele frequencies revealed four different $Kras^{G12D}$ gene dosage "states" (Fig. 2a, Extended Data Fig. 3c-h and Supplementary Table 9): focal gain ($Kras^{G12D\text{-}FG}$, 7.9%), arm-level gain ($Kras^{G12D\text{-}AG}$, 23.7%), copy number neutral loss of wt *Kras* ($Kras^{G12D\text{-}LOH}$, 36.8%) or no change ($Kras^{G12D\text{-}HET}$, 31.6%). Thus, two thirds of cancers had allelic imbalances causing increased $Kras^{G12D}$ gene dosage (hereafter designated $Kras^{G12D\text{-}iGD}$), suggesting strong selective pressure for its acquisition. In addition, two $Kras^{G12D\text{-}HET}$ tumors displayed loss of $Kras^{WT}$-mRNA, but high $Kras^{G12D}$ expression (blue dots in Fig. 2b), suggesting additional non-genetic mechanisms. Of note, we observed similar $KRAS^{G12D\text{-}iGD}$ rates/types in human PDAC cell lines (Supplementary Table 10). Gene dosage increase affects transcriptional output, as $Kras^{G12D\text{-}iGD}$ mPDAC had higher $Kras^{G12D}$ mRNA expression than $Kras^{G12D\text{-}HET}$ cancers (Fig. 2b and Extended Data Fig. 3i).

Ras/Raf signaling amplification was observed at different stages of mammary, intestinal or lung tumorigenesis18–21. To identify the stage of $KRAS^{MUT\text{-}iGD}$-acquisition in PDAC, we microdissected low-grade human pancreatic intraepithelial neoplasias (hPanIN) from 19 patients and performed amplicon-based deep sequencing of *KRAS* exon-2 (Fig. 2c and Supplementary Table 11/12). hPanIN with exon-2-mutated *KRAS* (20/40 hPanINs featured $KRAS^{G12}$ mutations) displayed frequent $KRAS^{MUT\text{-}iGD}$: $KRAS^{MUT}$ allele frequencies >50% occurred in 50%, 38% and 67% of *KRAS* exon-2-mutated hPanIN1a, hPanIN1b and hPanIN2, respectively. Given that healthy tissue "contamination" rates in microdissected PanINs ranged between 10-60%, $KRAS^{MUT\text{-}iGD}$ is likely to be even more frequent. In cases with close to 100% mutant read frequency, *KRAS* interphase FISH excluded false-positive $KRAS^{G12D\text{-}iGD}$ arising through chr12 monosomy (Extended Data Fig. 3l-n). Moreover, false-positive $KRAS^{MUT\text{-}iGD}$ through cross-"contaminating" hPDAC is excluded due to either (i) the large distance of selected hPanINs to associated cancers, (ii) distinct *KRAS* mutations in hPanINs and associated cancers, or (iii) $KRAS^{MUT\text{-}iGD}$ in IPMN-related hPanINs without invasive hPDAC. Altogether, these data suggest a critical role of $KRAS^{MUT\text{-}iGD}$ in early PDAC progression.

Looking at organ dissemination, we found a dramatically increased metastatic potential of *Kras*$^{G12D\text{-}iGD}$ cancers (OR 16.7; 95% CI 2.8-98.0; Fig. 2d): primary mPDACs with *Kras*$^{G12D\text{-}iGD}$ were mostly metastasized (20/26), whereas *Kras*$^{G12D\text{-}HET}$ mPDACs were predominantly non-metastatic (2/12). Thus, *Kras*$^{G12D\text{-}iGD}$ drives both early progression and metastasis. This dual role explains (i) early PDAC dissemination in humans and mice22 and (ii) the high incidence of human PDAC metastasis at diagnosis23. We also mined published data8,24 and invariably found *KRAS*$^{MUT\text{-}iGD}$ in human PDAC metastases. However, because *KRAS*$^{MUT\text{-}iGD}$ is present in the primary (early acquisition), its contribution to metastasis could not be recognized by primary/metastasis comparisons8.

Alternative oncogenic gains in *Kras*$^{MUT\text{-}HET}$ tumors

Among the 12 cancers without *Kras*^{G12D}-dosage gain, two cases had *Myc* amplifications and two had *Yap1* gains (Fig. 2e and Extended Data Fig. 4a-d). *MYC* and *YAP1* are known human oncogenes, amplified in 12% (13/109) and 1% (1/109) of hPDAC, respectively (Fig. 2f). In addition, chr19 gain occurred more frequently in *Kras*$^{G12D\text{-}HET}$ (3/12) than *Kras*$^{G12D\text{-}iGD}$ tumors (4/26), although this was not significant. A focal amplification on chr19 contained 20 genes (Extended Data Fig. 4e). Cross-species analyses revealed frequent gains of the syntenic region in hPDAC, with two genes in the minimal peak region: *NFKB2* and *PSD,* both amplified in 7% (8/109) of hPDAC (Extended Data Fig. 4f). *NFKB2* (but not *PSD*) is expressed in human pancreas and hPDAC (Extended Data Fig. 4g,h), suggesting *Nfkb2* to be the target proto-oncogene on murine chr19. *NFKB2* mediates non-canonical Nfkb signaling. It has not yet been associated with hPDAC, but promotes cell cycle progression *in vitro*25, and knockout of its interaction partner *RelB* impairs PanIN formation in PK mice26. Thus, upon *Kras* mutation, further amplification of partial aspects of *Kras* downstream signaling (*Myc*, *Yap1* or *Nfkb2*) seem sufficient to drive early PDAC progression, whereas strong metastatic potential is linked to amplification of the full *Kras*^{G12D} signaling program.

Evolutionary licensing of oncogenic dosages

The most frequent deletion in mPDAC affected *Cdkn2a* and/or the adjacent non-coding *Cdkn2a*-regulatory region *Ncruc*: 23 *Cdkn2a*$^{\Delta HOM}$, 4 *Ncruc*$^{\Delta HOM}$, 10 *Cdkn2a*$^{\Delta HET}$, 1 *Cdkn2a*^{WT} (chr4 alteration types shown in Fig. 3a,b, Extended Data Fig. 5a-d and Supplementary Table 9). Notably, the majority of *Cdkn2a/Ncruc*$^{\Delta HOM}$ cancers were *Kras*$^{G12D\text{-}iGD}$ (23/27) and had high *Kras*^{G12D} expression. In contrast, *Cdkn2a*$^{\Delta HET}$ or *Cdkn2a*^{WT} cancers were predominantly *Kras*$^{G12D\text{-}HET}$ (8/11) with low *Kras*^{G12D} expression (Fig. 3c, Extended Data Fig. 3j and 5e,f). Accordingly, in microdissected human PDAC datasets6, *KRAS*^{MUT} variant allele frequencies were higher in *CDKN2A*$^{\Delta HOM}$ than in *CDKN2A*$^{\Delta HET/WT}$ tumors (Fig. 3d and Extended Data Fig. 5g). Thus, *CDKN2A*$^{\Delta HOM}$-deletion and *KRAS*$^{MUT\text{-}iGD}$ are linked, with two possible scenarios: (i) *KRAS*$^{MUT\text{-}iGD}$ occurs first, but induces senescence that prevents progression until *CDKN2A* is lost (as proposed in breast tumorigenesis18), or (ii) *KRAS*$^{MUT\text{-}iGD}$ is only tolerated if preceded by *CDKN2A* deletion.

To resolve the sequence, we determined copy-number changes and copy-number neutral allelic imbalance at *Cdkn2a* and *Kras* in $Cdkn2a^{\Delta HOM}$;$Kras^{G12D\text{-}iGD}$ mPDACs (n=13) and associated metastases (n=25). We found identical *Cdkn2a* deletions in all 13 primary/metastasis pairs, but discordant chr6 CNA/LOH phenotypes in 7/13 pairs (Fig. 3e). In 6/13 pairs the sequence of *Cdkn2a-loss/*$Kras^{G12D\text{-}iGD}$ could not be reconstructed, either because the SNP density was too low (4 cases) or because chr6 profiles in primary/metastasis pairs were identical (2 cases). Thus, in all cases with reconstructable sequence, *Cdkn2a* deletion preceded $Kras^{G12D\text{-}iGD}$ acquisition. For example, mPDAC-53704 (Extended Data Fig. 6) had two liver metastases with identical *Cdkn2a* deletions, but distinct chr6 SNP patterns: one with $Kras^{G12D\text{-}LOH}$ at distal chr6 (through mitotic recombination) and another affecting the whole chromosome (likely through missegregation). This confirms clonal chr6 diversification and convergent evolution following *Cdkn2a* loss, and explains the primary´s gradual chr6 SNP pattern (Extended Data Fig. 6). Fig. 3f shows another example: mPDAC 5320 and its three metastases had identical *Cdkn2a* deletions, but distinct chr6 patterns: while liver metastasis-1 had $Kras^{G12D\text{-}AG}$ (combined interpretation of aCGH and SNP data), liver metastasis-3 and the lung-metastasis had distinct $Kras^{G12D\text{-}LOH}$ events, again showing convergent evolution of *Kras*-allelic imbalance and explaining the primary´s composite SNP pattern (Fig. 3f).

These results reveal several evolutionary principles in PDAC. First, $Kras^{G12D\text{-}iGD}$ is contingent on $Cdkn2a^{\Delta HOM}$ inactivation. Second, *Myc, Yap1 or Nfkb2* amplifications can occur on a $Cdkn2a^{\Delta HET}$ context, suggesting context-dependent *Cdkn2a* haploinsufficiency. Of note, only one cancer was $Cdkn2a^{WT}$. Third, evolution of multiple independent $Kras^{G12D}$-gains in $Cdkn2a^{\Delta HOM}$ cancers demonstrates functional convergence towards $Kras^{G12D\text{-}iGD}$ acquisition upon homozygous *Cdkn2a* loss.

To provide *in vivo* evidence for functional convergence in $Cdkn2a^{\Delta HOM}$ contexts, we generated mice with pancreas-specific $Kras^{G12D}$-expression and *Cdkn2a*-deletion (PKC). We found $Kras^{G12D\text{-}iGD}$ in 100% (16/16) of PKC tumors (Fig. 4 and Supplementary Table 9), confirming that $Kras^{G12D\text{-}iGD}$ acquisition is the preferred evolutionary route upon homozygous *Cdkn2a* loss.

Another hPDAC hallmark is *TP53* inactivation27. The analysis of cancers from $Kras^{G12D\text{-}Panc}$;$Trp53^{\Delta Panc}$ (PKP) mice revealed ubiquitous $Kras^{G12D\text{-}iGD}$ (16/16) (Fig. 4 and Supplementary Table 9). Thus, *Trp53*-loss (like $Cdkn2a^{\Delta HOM}$ alteration) predisposes to $Kras^{G12D\text{-}iGD}$ acquisition (also reflected in hPDAC; Extended Data Fig. 5g). PK/PKC/PKP cross-comparisons revealed higher CNA numbers and a tendency to amplify $Kras^{G12D}$ through arm-level gain (trisomy) in PKP, whereas copy-number neutral LOH predominates in PKC (Fig. 4 and Extended Data Fig. 5h). Of note, PKP or PKC tumors did not have complex chr4 rearrangements, confirming that chromothripsis in PK cancers results from natural selection for *Cdkn2a* inactivation (Fig. 4).

To address the role of the TGFβ-pathway, we characterized $Kras^{G12D\text{-}Panc}$;$Tgfbr2^{\Delta Panc}$ (PKT) mice (Fig. 4 and Supplementary Table 9). Strikingly, all PKT tumors (n=12) had *Cdkn2a* alterations: two cancers were $Cdkn2a^{\Delta HOM}$/$Kras^{G12D\text{-}iGD}$, ten were $Cdkn2a^{\Delta HET}$ and predominantly $Kras^{G12D\text{-}HET}$ (8/10). Overall, the prevalence of $Kras^{G12D\text{-}iGD}$ is

significantly lower in PKT (4/12) than PK mice (26/38) (P=0.04, Fisher's exact test, OR 0.23, 95% CI 0.06-0.92). *Kras*$^{G12D\text{-}HET}$ cancers had frequent alternative oncogenic gains (*Nfkb2*/chr19 trisomy in 4/8 PKT mice), similarly to *Kras*$^{G12D\text{-}HET}$ cancers in the PK cohort. Thus, contrary to *Trp53*$^{\Delta HOM}$ or *Cdkn2a*$^{\Delta HOM}$ alterations, which license *Kras*$^{G12D\text{-}iGD}$-acquisition, *Tgfbr2* alterations facilitate the alternative route with *Cdkn2a* haploinsufficiency.

Altogether these data show that evolutionary contingencies and convergence shape early tumorigenesis: different tumor suppressor genes/pathways (*Cdkn2a*, *Trp53*, Tgfβ), their alteration types (ΔHOM/ΔHET) or their combinations (e.g. *Cdkn2a*$^{\Delta HET}$/*Tgfbr2*$^{\Delta HET}$) direct evolution into different trajectories by licensing distinct types and extents of oncogenic dosage gains.

Integrating genomes, transcriptomes, phenotypes

Unbiased hierarchical clustering of RNA-Seq data from mPDAC cell cultures (PK cohort) revealed two clusters C1/C2, with 3 sub-clusters within C2 (Fig. 5a). Pathway analyses identified "epithelial cell differentiation" as the top C2 GO-term, whereas "mesenchymal cell differentiation" was defining C1 (Fig. 5a,b and Supplementary Table 13,14). Notably, all C1 cell lines show mesenchymal cell morphology, while C2 lines are invariably epithelial (Fig. 5a,c).

Previous studies classified human pancreatic cancer based on transcriptional profiles7,28,29. Unbiased hierarchical clustering with published classifiers shows large overlaps of subtypes proposed by Bailey7 and Moffitt29 to the initially proposed three Collisson28 subtypes: classical, exocrine-like, quasimesenchymal (QM). One exception is the lacking exocrine-like signature in the Moffitt classification, which was proposed to be an artefact of acinar cell "contamination" (details in Extended Data Fig. 7a-d). The Collisson classifier28 separates human PDAC cell lines into two subtypes (classical and QM; Extended Data Fig. 7e) and mouse PDAC cell lines into 3 subtypes: classical-equivalent, QM-equivalent (both in epithelial C2) and the mesenchymal M subtype (C1) (Extended Data Fig. 7f). The equivalent of the mouse M subtype with the strong EMT signature has not been described in human cell lines so far, reflecting underrepresentation of mesenchymal phenotypes in human cell line collections (see also Extended Data Fig. 7g,h). As described below, however, mesenchymal mPDACs in C1 represent undifferentiated pancreatic carcinomas with a pronounced EMT signature and human equivalent.

C1 shows strong gene set enrichment for Ras downstream signaling pathways (Fig. 5b and Supplementary Tables 13,14). This cannot be explained by the genetic *Kras* status alone: only C2a is *Kras*$^{G12D\text{-}HET}$, whereas C2b, C2c and C1 are mostly *Kras*$^{G12D\text{-}iGD}$. However, integration of *Kras*^{G12D} expression revealed its gradual increase from C2a to C2b/c and further substantial elevation in C1 (Fig. 5d and Extended Data Fig. 3k). Thus, the mesenchymal phenotype is associated with *Kras*^{G12D} expression above a certain threshold.

To study this association further, we induced clonal PDACs by CRISPR/Cas9 somatic mutagenesis30 in PK mice (Fig. 5e), screened for simultaneous presence of epithelial and

mesenchymal cells, and separated/enriched either phenotype by differential trypsinization. Two such cancers were identified. In each case, indel patterns of epithelial/mesenchymal pairs were identical (Extended Data Fig. 8a,b), showing (i) common clonal origin of epithelial/mesenchymal cells and (ii) independence of epithelial/mesenchymal phenotypes form CRISPR/Cas9-induced TSG alterations. Notably however, mPDAC 021 had $Kras^{G12D\text{-}iGD}$, elevated *Kras* expression and downstream pathway activation in mesenchymal, but not epithelial cells. In mPDAC 901 both clones were $Kras^{G12D\text{-}HET}$, but mesenchymal cells had increased *Kras* expression, supporting a role of $Kras^{G12D}$ dosage-variation in shaping cellular phenotypes (Fig. 5e, Extended Data Fig. 8c,d and Supplementary Table 15). Moreover, $KRAS^{G12D}$ overexpression in hPDAC cell lines induced an EMT signature, with Vimentin upregulation and E-cadherin repression (Extended Data Fig. 8e-g and Supplementary Table 16).

PDAC histology revealed a striking association with transcriptome clusters (Fig. 5a,f). Histopathologic grade scores increased from C2a to C2b/c and C1, with C2a being well- or moderately differentiated (G1, G2) and C1 being almost exclusively undifferentiated. Undifferentiated cancers are typically advanced and therefore underrepresented (1-3%) in human surgical series or cell line collections, but autopsy series reported up to 16% hPDACs with at least focal undifferentiated components31,32. Dedifferentiation can occur during disease progression or is triggered by treatment. It is associated with poor prognosis32,33, which is also reflected in mice (Extended Data Fig. 9a). Our results link this aggressive PDAC subtype with highest $Kras^{G12D}$ expression levels and Ras-related transcriptional programs (Fig. 5b,d and Supplementary Table 13). We also screened human transcriptome data (ICGC PACA-AU cohort) for undifferentiated pancreatic carcinomas and performed unbiased hierarchical clustering of differentially regulated genes in undifferentiated cancers (Extended Data Fig. 9b). Of note, undifferentiated human pancreatic carcinomas are characterized by reduced expression of genes involved in “epithelial” (cluster-2) or “squamous differentiation” (cluster-1), and a strong upregulation of genes in cluster-3, containing gene sets enriched for EMT and Ras downstream signaling (Extended Data Fig. 9b-d and Supplementary Table 17 and 18).

We exploited the mouse to address complex questions, including cell based resources (overcoming human PDAC´s stroma richness), primary/metastasis resources (phylogenetic tracking, evolution) and *in vivo* modelling (proof-of-concept functional studies). In addition, discoveries were facilitated by the relatively low complexity of mouse PDAC genomes (easier interpretability). Notably, a transposon-induced PDAC model13 showed that our findings are equally valid in contexts of excessive mutational loads (Extended Data Fig. 10 and Supplementary Table 19).

Conclusions

Our study proposes a novel comprehensive conceptual framework for molecular PDAC evolution and phenotypic diversification. It describes evolutionary trajectories, identifies their genetic hallmarks and shows how oncogenic dosage-variation is differentially licensed along individual routes by the three major PDAC tumor suppressive pathways to control critical disease characteristics, including early progression, histopathology, metastasis,

cellular plasticity and clinical behavior (Fig. 5g). *RAS* gene mutations affect more than 30% of human cancers, often involving their allelic imbalance. We therefore presume that the principles identified here are significant far beyond PDAC.

Methods

Primary mPDAC cultures preparation

For 2D primary cell culturing, primary tumor or metastasis were cut into small pieces and digested 1-2h in 200Units/mL collagenase II (Worthington) in DMEM medium (Thermo Fisher Scientific Inc.) containing 10% fetal calf serum (FCS, Merck) and 1x Penicillin/ Streptomycin (P/S, Thermo Fisher Scientific Inc.). After short term expansion, primary cells were frozen in 10% dimethyl sulfoxide (Roth) and 50% FCS. For all primary culture experiments, culturing medium (DMEM supplemented with 10% FCS and 1x P/S) and cultures with less than 10 passages were used. Primary cultures were routinely tested for mycoplasma contamination by PCR and authenticated by re-genotyping of cell cultures and corresponding mice.

gDNA and RNA isolation

gDNA from murine primary cell culture pellets was isolated using the DNeasy Blood & Tissue Kit (Qiagen) according to manufacturer's instructions. Total RNA was isolated with the RNeasy kit (Qiagen) from 60-80% confluent primary cell lines cultured in a 10cm dish in culturing medium without P/S and immediately transferred into RLT buffer (Qiagen) containing ß-mercaptoethanol.

Histology and micro-metastases screening

For histologic characterization of mPDACs, 2µm thick specimens from formalin-fixed paraffin embedded (FFPE) material were routinely H&E stained and submitted to two veterinary pathologists experienced in comparative pancreatic cancer pathology. Histopathologic grading was performed with respect to the most recent consensus report of genetically engineered mouse models34. For histopathologic examination of micro-metastases, three H&E-stained liver sections (separated by 200µm) were screened for metastatic lesions by a veterinary pathologist.

Animal experiments

Mice were maintained on *C57Bl/6;129S6/SvEv* mixed background and housed under specific-pathogen-free conditions. Female and male mice were randomly submitted to respective tumor cohorts. For the generation of double- or triple-mutants, pancreas-specific Cre lines10,35,36 were intercrossed with $Kras^{G12D\text{-}Panc}$ (PK mice)9,10 only, or in addition with $Cdkn2a^{\Delta HOM\text{-}Panc}$ (PKC mice)37, $Trp53^{\Delta HOM\text{-}Panc}$ (PKP mice)38,39 or $Tgfbr2^{\Delta HET\text{-}Panc}$ and $Tgfbr2^{\Delta HOM\text{-}Panc}$ (PKT mice)40 mice. Kaplan-Meier survival curves were generated using Prism (GraphPad Software v5.01). In case the animal presented a palpable abdominal mass above 1.5cm, ascites, signs of sickness or a weight loss of more than 15% of the body weight, mice were euthanized in compliance with the European guidelines for the care and use of laboratory animals. For necropsy of tumor-bearing mice, the abdominal cavity was macroscopically checked for pancreatic cancer and for metastases

at the main metastatic routes (liver, lung, lymph nodes). Animal studies were approved by the Institutional Animal Care and Use Committees (IACUC) of Technische Universität München (Regierung von Oberbayern, Munich, Germany).

Amplicon-based deep sequencing at the *Kras* locus or of *Kras* mRNA

Fifty ng of high-quality genomic DNA or reversely transcribed mRNA (cDNA) were subjected to amplicon-based deep sequencing. Briefly, the $Kras^{G12D}$-mutated locus was amplified using Q5® High-Fidelity DNA Polymerase (New England Biolabs, 40 cycles) and primers with Nextera adapter overhangs (Supplementary Table 20). In a second Q5® PCR step (15 cycles), Nextera index primers (Illumina) were added. After each PCR step, solid phase reversible immobilization cleanup (0.8x) was performed using the Agencourt® AMPure® XP kit (Beckman Coulter GmbH). The pooled library was quantified by SYBR® Green qPCR (Thermo Fisher Scientific Inc.) and the Kapa Biosystems library quantification kit. In total, 8pM of denatured library (20% spiked PhiX DNA) was sequenced in 300bp paired end mode using a MiSeq system (Illumina). Raw reads were mapped to *Kras* reference sequence (Ensemble release GRCm38p4, Genome Reference Consortium). Variant allele frequencies on chr6 at position 145246771 were calculated.

Microdissection of hPanIN and $KRAS^{G12}$ status analysis

Nineteen patients (Supplementary Table 11) with or without a history of pancreatic cancer were included into hPanIN lesion analysis, according to approval by the Ethics Committee of the Faculty of Medicine of the Technische Universität München. Patients were classified using WHO recommendations and the TNM staging system. Serially cut 10μm thick specimens from FFPE material were air-dried overnight. Paraffin was removed through short incubation with xylene. Specimens were briefly stained with hematoxylin and kept wet for the micro-dissection procedure. Individually diagnosed samples were microdissected under the Axio Imager microscope (Zeiss) using 20 gauche cannula. Pre- and post-sampling microscopic pictures were taken to (i) document dissection performance and (ii) re-identify each specimen on the corresponding H&E-stained slide. gDNA was extracted as described above using MinElute spin columns (Qiagen) for higher sample concentration. Five μl of eluted hPanIN gDNA were submitted to amplicon-based deep sequencing of *KRAS* exon-2 for detection of $KRAS^{G12}$ hotspot mutations. Briefly, 2 pairs of custom *KRAS* primers (Supplementary Table 20) were used for nested PCR amplification of the corresponding *KRAS* region. Illumina Nextera primer pairs were used to add sequencing adapters and indices. PCR steps, library quantification and sequencing were performed as described above. Raw reads were mapped to *KRAS* reference sequence (GRCh38.p10). Variant allele frequencies were calculated for $KRAS^{G12}$ hotspot mutations (positions 25398284 and 25398285 on chr12).

Whole genome sequencing (WGS)

One μg of high-quality gDNA extracted from primary tumor cell line and corresponding tail were sheared on a Covaris M220 focused ultrasonicator (Covaris, Inc.) to an approximate fragment size of 500bp. Library was prepared from 500ng of fragmented gDNA using the NEBNext® Ultra™ II DNA Library Prep Kit (New England Biolabs, Inc.) in combination with the adapter/primer sequences and PCR conditions published before41. The final library

was quantified by qPCR using the Kapa Biosystems library quantification kit. Equimolar amounts of indexed libraries were denatured and diluted to a final concentration of 1.8pM and sequenced in 300bp paired end mode on a NextSeq 500 system (Illumina) to ~20x coverage. Sequencing raw data were converted to fastq format using the bcl2fastq software v2.18.0.12 (Illumina). Raw reads were trimmed with Trimmomatic v0.36 to preserve an average base Phred quality of 25, mapped using the BWA-MEM algorithm v0.7.12 with alternative contig handling and mapped to GRCm38.p5 reference genome.

Inference of chromothripsis

For estimation of copy number states, the Bioconductor HMMcopy package 1.16.0 was used followed by segmentation with the Bioconductor DNAcopy package 1.48.0. For LOH analysis variant positions in control and tumor were computed with samtools mpileup v1.3.1. Only positions in regions with mapping quality of 60 and an average phredscore of 20 were considered for further analysis. Furthermore, positions harboring strand bias and variant allele frequencies less than 20% and above 85% in the control were excluded as they are likely homozygous in the germline. The minimal cutoff coverage for a given polymorphic position in the control was set to eight reads. Segmental duplications (UCSC Genome Browser) and regions with mouse line specific variation (Mouse Genomes Project, REL-1505) were excluded. For this set of somatic nucleotide polymorphisms (SNPs) the difference of frequencies between tumor and control samples were calculated. DELLY v0.7.6 was used for calling structural variations (SVs). SV-classes were defined according to DELLY callings: Deletion-type (3to5), duplication-type (5to3) and inversion-type (5to5 and 3to3). The predicted rearrangements were merged and filtered based on variant frequency, mapping quality and the distance between two connected breakpoints. The existence of chromothripsis was tested by applying the six hallmark criteria proposed by Korbel *et al.*14. Clustering of SV breakpoints was tested using a χ^2-goodness-of-fit test. Regularity of oscillating copy number states in the chromothriptic model was compared to a virtual chromosome generated by a Monte Carlo simulation, as described in42. For each distinct number of breakpoints, 100 simulation runs were completed and mean values as well as 95% CI were calculated. Interspersed loss and retention of heterozygosity was analyzed by calculating the Jaccard index between heterozygously deleted segments and regions comprising LOH and SNP information. Randomness of observed DNA segment order was tested using a Monte Carlo simulation as described in14. The uniform distribution of SV-types was tested using a χ^2-goodness-of-fit test. The Wald-Wolfowitz runs test as implemented in R package randtests 1.0 was performed for testing right-sided against the null hypothesis of randomly distributed 5'-to-3' breakpoint joints sequence.

FISH analyses

For the analysis of copy number status or large structural alterations of human and murine primary cell lines, multicolor fluorescence in situ hybridization (M-FISH) was performed as described before43. For *KRAS* gene detection in hPanIN specimens, the Zyto*Light*® SPEC KRAS/CEN12 Dual Color Probe kit was used according to manufacturer's instructions (ZytoVision GmbH). In brief, 2μm FFPE specimens were deparaffinized, pre-incubated in CC 2 buffer (at 95°C for 24min), treated with pepsin solution (at 37°C for 8min) and denatured by a heat treatment step at 80°C for 8min on an automated Discovery XT system

(Ventana Medical Systems, Inc.). KRAS/CEN12 dual color probe hybridization was performed by co-denaturing at 75°C for 10min and by incubating at 37°C overnight in a ThermoBrite system (Abbott Laboratories). Slides were washed, nuclei stained with 4',6-diamidino-2-phenylindole (DAPI), covered in an antifade mounting medium and by a coverslip and stored for confocal laser scanning microscopy (LSM) analyses at 4°C in the dark. Zyto*Light*® SPEC KRAS/CEN12 Dual Color Probes and DAPI nuclear stain (excitation/emission: DAPI 405nm/415-490nm; ZyGreen, 503nm/510-540nm; ZyOrange, 547nm/560-650nm) were detected by confocal LSM using a Leica TCS SP8; DMi8 CS microscope equipped with a 63x/1.4 oil immersion objective (Leica). Images (z-stacks, covering the whole nucleus) with a magnification factor of 3 and a frame size of 2048 x 2048 pixels were collected. Generated images were processed using the Huygens Essential software (Scientific Volume Imaging) for deconvolution, than merged and maximum projections were converted with Leica LAS X software.

aCGH analysis

Agilent oligonucleotide aCGH (SurePrint G3 Mouse CGH 240K or custom 60K microarray) was performed according to manufactures instructions. Agilent Genomic Workbench software v7.0.4.0 was used for aCGH data preprocessing. Legacy centralization option was used for re-centralization of raw log ratios to the most common ploidy state. ADM-2 algorithm was applied for aberration calling. Segments coordinates were reported for GRCm37 reference genome. Aberrations on chromosome 6 between positions 148719747 and 149503634 were excluded in further downstream analysis as this region resulted likely from an artefact. Normalized and curated data was imported into R.

Whole-exome sequencing (WES) analysis

Coding exons were enriched via whole-exome pull down using Agilent SureSelect Mouse Exon Kit according to manufacturer's instructions and sequenced on the Illumina HiSeq2000 system. Prior to mapping, raw sequencing reads were trimmed using Trimmomatic v0.33. Leading and trailing bases with phred scores below 25 and reads shorter 50 nucleotides were removed. In addition the average base quality within a sliding window of 10 nucleotides should be above 25 to keep the read for further downstream analysis. Reads were aligned to the GRCm38.p3 reference genome using BWA-MEM 0.7.12 with default settings. PCR duplicates were marked with Picard tools v1.130 and realignment around indels was performed with GATK toolkit v 3.4.46. Mutect v 1.1.7 was used for calling somatic mutations with default settings. Potential somatic events were filtered for SNPs by excluding SNVs which were listed in in release 1505 of the Mouse Genome Project SNP database44. Somatic point mutations were included in the final list, if the read coverage for each position was ≥10 in both control and tumor, variant frequency was ≥10% and read count supporting the variant nucleotide is ≥3 in the tumor sample and =0 in the control. Further, SNVs marked as strand or PCR bias artifacts by “DKFZBiasFilter” (https://github.com/eilslabs/DKFZBiasFilter, using default settings) or with a FOXOG-Score of 1 were excluded. Annotation of somatic events was conducted with SNPeff v4.1. SNVs causing variation in splice sites or upstream/downstream of genes were excluded from further analysis. Indels were detected with Pindel45. For each potential indel the read coverage was re-calculated using bedtools v2.17.0. Criteria for further downstream processing were: Variant frequency

≥10% in tumor and =0% in control; and total coverage at the altered position in both control and tumor ≥20. LOH analysis was conducted as described in chapter Inference of Chromothripsis.

WES data analysis from hPDAC

Mapped BAM files from Witkiewicz *et al.*6 were downloaded from the Sequence Read Archive (accession number PRJNA278883) approved by the Ethics Committee of the Faculty of Medicine of the Technische Universität München. Further downstream analysis was performed as described above. SNPs were filtered by excluding variants with an alternate allele frequency ≥1% in the 1000 Genomes Project, as listed in dbSNP build 146. All available VCF files from the TCGA-PAAD cohort generated by Mutect2 were downloaded from the NIH Genomic Data Commons data. Downstream processing was performed as described above (PCR and strand bias marking by DKFZBiasFilter was not possible using VCF files). SNPs were filtered by excluding variants with an alternate allele frequency ≥1% in the 1000 Genomes Project, as listed in dbSNP build 142. MAF files from other human pancreatic cancer cohorts were downloaded and included in our analysis: All samples, for which whole-exome sequencing data was available, as provided by Bailey *et al.* 7; pancreatic cancer cell lines from the Cancer Cell Line Encyclopedia46 and SNV data from pancreatic cancers as analyzed by Alexandrov *et al.*47. In these cohorts, SNPs were filtered by excluding variants with an alternate allele frequency ≥1% in the 1000 Genomes Project, as listed in dbSNP Build 146. Remaining SNVs were annotated and filtered with SNPeff as described above.

Analysis of mutational signatures

Mutation spectra for each cohort were compared to a list of 21 signatures previously described by Alexandrov *et al.*47; Signature 1B was excluded from further analyses because of presumed biological similarity to Signature 1A. The contribution of each individual signature to the mutation spectrum of each cohort was analyzed by using “deconstructSigs” v1.8.0.

qRT-PCR analysis

Reverse transcription was performed with random hexamers using 1μg of total RNA following instructions of the SuperScript II protocol (Thermo Fisher Scientific Inc.). Real-time qPCR was performed either with the TaqMan qPCR chemistry (Thermo Fisher Scientific Inc.) for mouse using *Kras*-specific primers and probes or with the SYBR® Green master mix (Thermo Fisher Scientific Inc.) using primers for human target genes *VIM*, *CDH1* and *MMP1* (Supplementary Table 20). *Gapdh* or *GAPDH* in combination with *PPIA* were used as housekeeping genes for normalization (Supplementary Table 20). qPCR was conducted on a StepOnePlus system (Applied Biosystems). For analyses of mutant $Kras^{G12D}$ mRNA levels in mPDACs, first total (wild-type plus mutant) *Kras* mRNA levels were determined using qRT-PCR. Second, the identical cDNA was used for amplicon-based deep sequencing to detect the proportion of mutant to wild-type *Kras* mRNA. Third, the mutant to wild-type *Kras* mRNA ratio was multiplied with the total *Kras* mRNA level to calculate the mutant $Kras^{G12D}$-specific mRNA level.

RNA-Seq analysis

Bulk 3'-prime transcript end RNA-Seq (SCRB-Seq) libraries were prepared as described previously48. Briefly, RNA was reversely transcribed using oligo-dT primers decorated with sample barcodes, unique molecular identifiers (UMIs) and adapters (Integrated DNA Technologies). cDNA from all samples was pooled and un-incorporated primers digested using ExonucleaseI (New England Biolabs). Next, the cDNA pool was amplified with KAPA HiFi ReadyMix (KAPA Biosystems). To obtain sequencing libraries, 0.8ng of cDNA was tagmented and 3' ends amplified with the Nextera XT Kit (Illumina) using a specific primer for the adapter on the 3'-end. The library was paired-end sequenced on a HiSeq1500 with 16 cycles for read 1 to decode sample barcodes and UMIs and 51 cycles on read 2 into the cDNA fragment. For the preparation of the human pancreatic cancer cell line samples, the flow cell binding sites P5 and P7 were exchanged to allow sequencing of the cDNA in read1 and barcodes and UMIs in read2. Data was processed using the published Drop-seq pipeline (v1.0)49 to generate sample- and gene-wise UMI tables. Reference genome (GRCm38) was used for alignment. Transcript and gene definitions were used according to the ENSEMBL annotation release 75. Further analyses were performed with R version 3.2.2. Initial hierachical clustering (method: Complete linkage, distance measure: Euclidian) of samples was performed for the top 10% variable genes. Bootstrapping was performed to access cluster stability with the pvclust package v2.0. The 4 most prominent clusters were selected and differential expression between these clusters was calculated with DEseq250. A gene was considered to be differentially regulated if the absolute log2-foldchange was above 0.8 and the adjusted P-value was ≤0.05. Gene set enrichment testing was performed with DAVID 6.851 or the hypergeomtric test as implemented on the "Molecular Signature Database" (MSigDB) v6.0 homepage (http://software.broadinstitute.org/gsea/msigdb/annotate). For all MSigDB analyses, top100 enriched terms with a false discovery rate (FDR) of $P \leq 10^{-4}$ were included. Published PDAC classifier genes28 and the hallmark EMT gene set (downloaded from MSigDB v5.252) were used for sample clusterings (method: Ward, distance measure: Euclidian).

hPDAC subtyping

Normalized RNAseq data was derived from Bailey *et al.*7. Samples that were histologically classified as "PDA-Adenosquamous carcinoma" and "Pancreatic Ductal Adenocarcinoma" were used for hierarchical clustering (method: Ward, distance measure: Euclidian) with classifier gene lists published elsewhere28,29.

Microarray data analysis

Affymetrix-based CCLE raw data set was downloaded from (Broad-Novartis Cancer Cell Line Encyclopedia, Version 2.17). Hematopoietic or lymphoid neoplasms were excluded since (1) the primary interest of our study were solid tumors and (2) the overall gene expression signature of these samples was shown to be very distinct from all other samples in the study46. Normalization of the data was performed with RMA. In general, if genes were represented by two or more probe sets, the probe set with the highest mean expression was used for all further microarray data analyses. Mapping between probeset and genes were conducted with the appropriate Bioconductor packages. Target genes for the *TP63ΔN*

network were downloaded from the “Pathway Interaction Database” (PID)53 and hierarchically clustered (method: Ward, distance measure: Euclidian). Gene set enrichment analysis was conducted with DAVID or MSigDB v6.0. All following microarray data sets are Illumina-based and were VST-transformed followed by quantile normalization as implemented in lumi54. Microarray data set of hPDAC cell lines (accession number GSE17891) was downloaded from Gene Omnibus Expression database. PDAC classifier genes and EMT hallmark gene set were used as described above. For the comparison of human wild-type pancreatic tissue and hPDAC cell lines, limma55 was used for detection of differential expression between groups. Differentially expressed genes were determined with an alpha level threshold of 5%. The PACA-AU ICGC data set was downloaded from the repository https://dcc.icgc.org/repositories. Samples that met the following criteria were selected for further analyses: (i) Bailey HistoSubtypes “PDA-Adenosquamous carcinoma” or “Pancreatic Ductal Adenocarcinoma” with available subtype information from Bailey *et al.*7 and (ii) ICGC WHO Grading “Undifferentiated carcinoma”. Only representative samples, as judged by cluster analysis, from this group were selected for downstream analysis. ANOVA was performed across six defined subgroups of pancreatic cancer: (i) undifferentiated pancreatic carcinoma, (ii) adenosquamous pancreatic carcinoma and (iii-vi) PDAC sub-stratified in pancreatic progenitor, immunogenic, squamous and ADEX subtypes. Genes with an adjusted P-value ≤0.05 were hierarchically clustered (method: Ward, distance measure: Manhattan) and the resulting cluster tree was computationally stratified into five sub-clusters. Genes within subclusters were used for gene enrichment analysis as described above. Seventeen PK-PB primary cultures established elsewhere13 were submitted to RNA extraction and subsequent gene expression profiling analysis on a MouseWG-6 v2.0 Expression BeadChip (Illumina). The 5% of genes with the highest variability across all samples were used for hierarchical clustering using the ward method for aggregation of samples. Limma was used as described above. A gene was called differentially expressed if the adjusted P-value was ≤0.05 and the log2-fold was at least 0.8.

Quantitative transposon insertion site sequencing (QiSeq)

Aforementioned gDNA samples of the PK-PB pancreatic cancer cell cultures13 were sequenced for transposon integration sites and bioinformatics analyses were performed as described elsewhere56. Transposon integration sites that are supported by at least 20 reads and reside in intragenic regions were counted for the computation of the mutational burden. For the assessment of the *Cdkn2a/Ncruc*$^{\Delta HOM}$ status caused by transposon insertional mutagenesis, only the top hit of each tumor was considered.

Kras^{G12D} induction after lentiviral transduction of hPDAC cell lines

The pINDUCER2057 vector system comprising a puromycin resistance gene was used for doxycycline-inducible *KRAS*^{G12D} overexpression. Briefly, cDNA of oncogenic *KRAS*^{G12D} (CCDS 8702.1, 35G>A) and *GFP* were cloned into the pINDUCER20 lentiviral vector. Stbl3™ (Thermo Fisher Scientific Inc.) were chemically transformed and pDNA sequence was verified. For lentivirus production, HEK293FT cells were transfected using *Trans*IT®-LT1 (Mirus Bio LLC) with standard virus packaging plasmids and respective pINDUCER20 vectors by following manufacturer’s recommendations. Virus-containing supernatant was pooled 48h and 72h post transfection, concentrated by polyethylene glycol 6000

precipitation58 and stored at -80°C after shock-freezing. $1x10^5$ HUPT3 (COSMIC ID: COSS907285) and PANC0327 (COSMIC ID: COSS925346) hPDAC cells were transduced in presence of 1μg/mL polybrene and selected with puromycin antibiotic. Target gene expression was induced for stated time points by the addition of 100ng/μL doxycycline into P/S-free culturing medium. RNA isolation, qRT-PCR and SCRB-Seq were performed as described above. For differential gene expression analysis, raw sequencing data were mapped to the human reference genome (GRCh 38p10). Transcript and gene definitions were used according to the ENSEMBL annotation release 87. Group comparisons (*KRAS*^{G12D} vs *GFP*) were conducted with DESeq2.

Somatic CRISPR/Cas9 gene-editing for tumor clone tracking in mice

Multiplexed gene editing of tumor suppressor genes using CRISPR/Cas9 in the pancreas of PK mice was performed as described elsewhere30. Primary cultures of induced mPDACs were isolated as described above and monitored for the simultaneous presence of epithelial and mesenchymal phenotypes. Enrichment of epithelial and mesenchymal cell morphologies was achieved by differential exposition times to trypsin (Thermo Fisher Scientific Inc.). Short-term incubation (2-3 min) at room temperature induced detachment of mesenchymal cells, while epithelial colonies remained adherent. Both cell fractions were subsequently grown to 80% confluency in new flasks. This process was repeated for 3-6 times until homogenous epithelial and mesenchymal cell fractions were enriched. Clonal origin of both phenotypes was confirmed by targeted amplicon-based next generation sequencing of CRISPR/Cas9-edited loci as described earlier30,59. Analyses of the *Kras* allelic status and mRNA expression were carried out as described above.

Statistics and reproducibility

For each experiment, all statistics were performed as indicated in respective Figure legends and Extended Data Figure legends. Statistical testing across all classes was performed to account for multiple testing. Continuous variables were tested for normal distribution. Non-parametric tests were used for non-normally distributed data. Complex statistical techniques are explained in detail in the Methods section. No animals were excluded from any of the cohorts. The veterinarian pathologists were blinded during histological grading of primary tumors and metastasis screening. The study was of explorative nature. Due to this study design prior knowledge of the expected effect-size was not available and no power calculations were conducted.

Code availability

Source code is available from the authors upon reasonable request.

Data Availability

Sequence data have been deposited at EBI European Nucleotide Archive (ENA; https://www.ebi.ac.uk/ena) under accession number PRJEB23787. Microarray data have been deposited in the Gene Expression Omnibus (GEO; https://www.ncbi.nlm.nih.gov/geo/) under accession number GSE107458. All data are available from the corresponding author upon reasonable request.

Europe PMC Funders Author Manuscripts

Extended Data

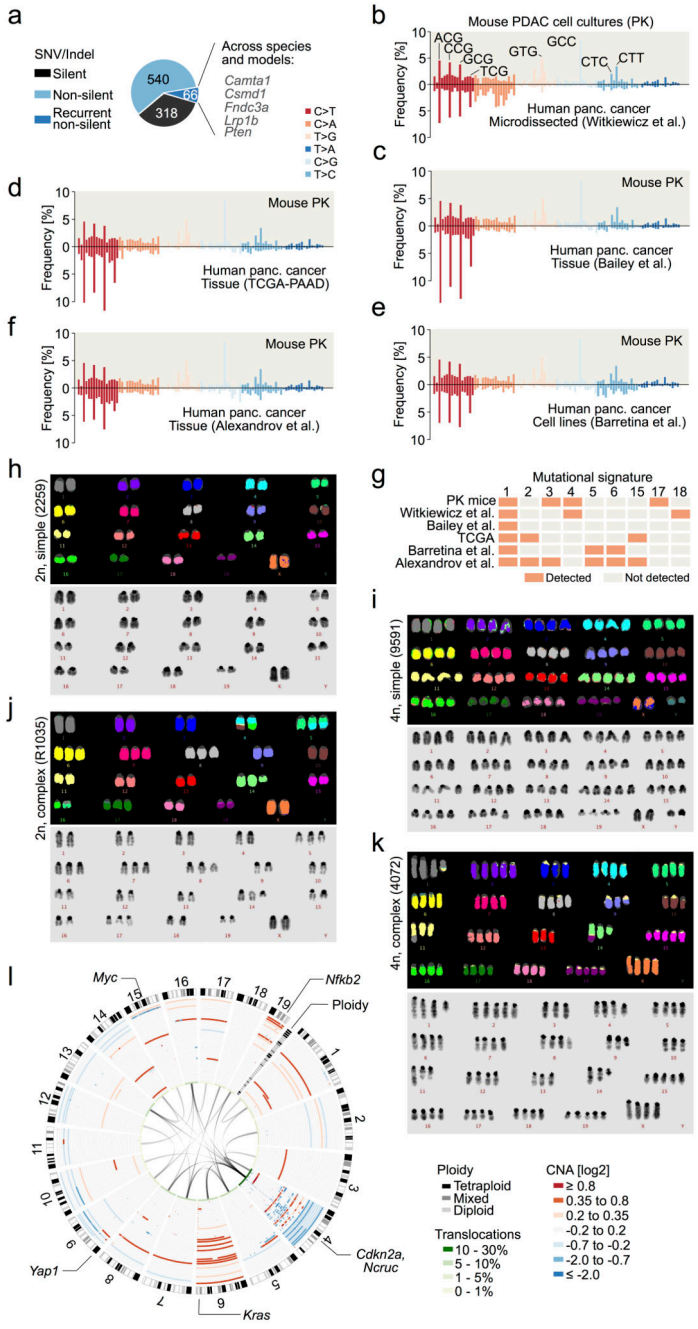

Extended Data Figure 1. Mutational patterns, karyotype complexity and structural alterations in primary PDAC.

a, Single nucleotide variants (SNVs) and indels in primary PDAC cultures derived from 38 *KrasG12D* (PK) mice, as detected by whole-exome sequencing. Recurrently mutated genes that are frequently altered in human cancers and/or genomewide pancreas-specific transposon screens are indicated. **b**, Frequency of somatic base substitutions based on trinucleotide context in mouse (n=38 PK mice) and human PDAC (n=51 patients, data used

for analysis from 6). **b-f**, Mutation spectra defined by trinucleotide contexts around base substitutions as detected by whole-exome sequencing show similar patterns in PK mice (n=38) and in relevant human pancreatic cancer cohorts. Base substitutions were extracted from BAM, VCF or MAF files from: **b**, Witkiewicz *et al.*6, **c**, Bailey *et al.*7, **d**, TCGA-PAAD, **e**, Barretina *et al.*46 and **f**, Alexandrov *et al.*47. Additional information regarding the analysis of each cohort is provided in Supplementary Table 2. **g**, Mutational signatures in mouse and human pancreatic cancer cohorts. Information on mutational signatures was used from Alexandrov *et al.*47, who identified 21 mutational signatures operative in human cancer. The „deconstructSigs“ tool was used to determine the composition of the given set of 21 mutational signatures in each pancreatic cancer cohort. Extraction of mutational signatures strongly depends on SNV load per tumor. Due to the low mutational burden of mPDACs from PK mice (median of 18 SNVs per tumor as detected by WES), the analyses of mutational signatures could not be performed at the level of individual tumors. We have therefore investigated the contribution of each of the 21 mutational signatures to the SNV spectrum at the cohort-level (see Methods). Signature 1, reflecting age-associated C>T transversions at NCG trinucleotides, was the only signature consistently identifiable in all cohorts of human and mouse pancreatic cancer. In comparison to human cohorts, PK mice show C>G substitutions at GCC trinucleotides that cannot be attributed to one of 21 mutational signatures. Note that mutations at the GCC motif are not a general phenomenon of PDAC from PK mice, since only 4 samples are predominantly contributing to this peak. **h-i**, Representative M-FISH karyotypes with no or few karyotypic changes are shown for a diploid (40 chromosomes) and tetraploid mouse PDAC (81 chromosomes). Tumor 9591 shows gain of chr14. **j**, Representative karyotype of a complex diploid mPDAC genome with aneuploidy and translocations (46 chromosomes). Both copies of chr4 are involved in translocations: der(4)t(4;10) and der(4)t(4;16); likely affecting *Cdkn2a.* Further structural alterations and copy number changes are: +5, der(5)t(4;5)*2, +6, +7, +8, del(9), +14, del(14), der(16)t(5;16), +17. **k**, Representative example of a complex tetraploid mPDAC karyotype (77 chromosomes). Structural alterations are: der(1)t(1;11), dic(9;9), der(11)t(1;11), and der(14)t(14;19). Single chromosomal copy number changes are: +2, -3, -9, -10, -11, -13, -14, +15 and +19. Del, deletion; der, derivative chromosome; dic, dicentric chromosome; t, translocation; „-“, chromosome loss; „+“, chromosome gain. **l,** (Extension to Fig. 1c.) Circos plot shows CNAs assessed by aCGH as well as translocations and ploidy states detected by M-FISH in 38 primary PDACs derived from PK mice (n=38). CNAs for each mPDAC are displayed as log2 difference from tail control. Frequencies of translocations per chromosome are indicated in green in the inner circle of the graph. Connecting lines indicate individual translocations and involved chromosomes. On chr4, genomic alterations frequently involve *Cdkn2a* or *Ncruc*, a Non-coding regulatory region upstream of *Cdkn2a* (27/38 cancers with homozygous and 10/38 with heterozygous inactivation of *Cdkn2a* and/or *Ncruc*). Only one cancer remained $Cdkn2a^{WT}$. The target of copy number changes on chr6 is $Kras^{G12D}$, either through arm level gain or focal amplification. In addition, primary mPDAC of PK mice exhibited recurrent genetic amplifications affecting other known oncogenes, such as *Myc* or *Yap1*, or *Nfkb2*, a novel oncogenic PDAC driver identified in this study (see also Fig. 2e,f and Extended Data Figure 4).

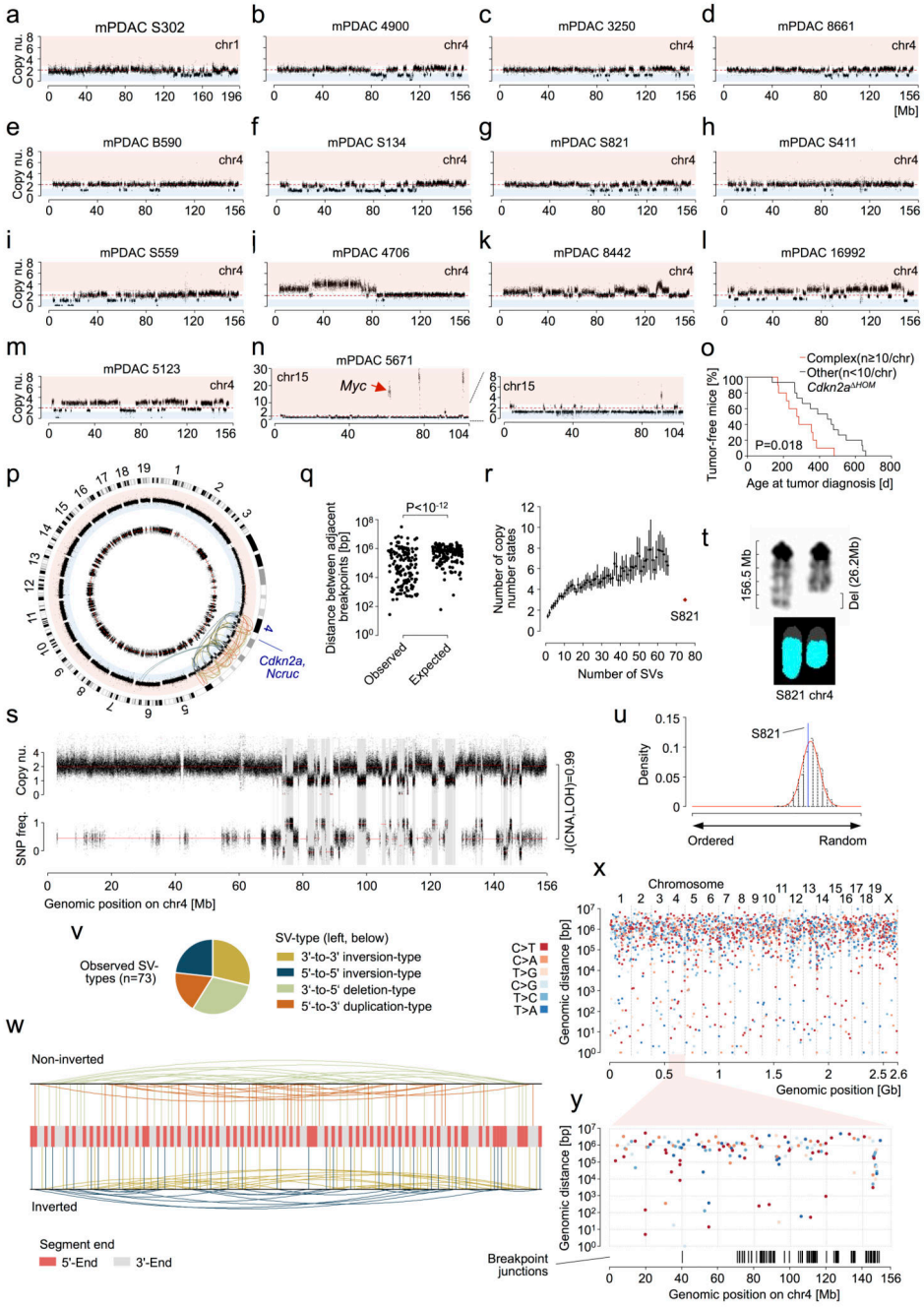

Extended Data Figure 2. Characterization of complex rearrangements in PDAC from PK mice and statistical inference of chromothripsis based on whole genome sequencing (WGS).

a-n, Copy number profiles of chromosomes with complex rearrangements (defined as n≥10 CNAs per chromosome) from primary mPDAC cell cultures as detected by aCGH. A total of 14 mPDACs had chromosomes with complex rearrangements. **a-i**, Nine primary mPDACs show copy number patterns characterized by heterozygous deletions and oscillation of copy number around few states, indicating chromothripsis as the underlying mechanism. **g**, mPDAC-S821 was subjected to whole genome sequencing for the inference of

Europe PMC Funders Author Manuscripts

chromothripsis using previously established criteria14 (see Fig. 1d and Extended Data Figure 2p-w). **j-m**, Four primary mPDACs showed complex rearrangements with multiple copy number states on chr4, likely acquired through progressive/sequential rearrangement cycles. **n**, Cancer 5671 carries a complex rearrangement on chr15 characterized by oscillating copy number states and 3 prominent focal amplifications, of which one contained the *Myc* oncogene. *Myc* amplification is most likely the result of double minute chromosome formation during chromothriptic rearrangement of chr15. **o**, Comparison of age at tumor diagnosis in $Cdkn2a^{\Delta HOM}$-deleted cancers with (n=10) or without (n=15) complex clustered chromosomal rearrangements (n≥10 CNAs/chromosome). Complex clustered rearrangements are associated with significantly shortened time to tumor diagnosis, indicating accelerated tumor evolution through genetic crisis. Two-sided log-rank test. **p**, Criteria proposed by Korbel *et al.*14 were tested for the inference of chromothripsis. Circos plot displays SNP ratio (inner circle, red dashed line indicating heterozygosity), CNV (outer circle, blue area indicating deletion, red amplification) and structural variations (SVs, colors as in v) as detected by WGS. Chr4 shows a complex deletion pattern and massive rearrangements associated with loss of one copy of *Cdkn2a*. The second copy of *Cdkn2a* is focally deleted. In addition, a balanced translocation of a ~200Kb segment from trisomic chr6 to chr4 and a far smaller segment of chr4 into chr6 was detected. The *Kras* locus is not directly affected by this inter-chromosomal translocation. LOH, CNAs and rearrangements are not detected on other chromosomes. **q**, In a chromothriptic model, DNA breakpoints tend to cluster on a chromosome. Testing against an exponential distribution (parameter λ derived from mean of observed distance between adjacent breakpoints), revealed significantly shorter distances than expected in a progressive model (n=146 breakpoints). $P<10^{-12}$; χ_-goodness-of-fit test. **r**, In a progressive model of acquisition of massive rearrangements, copy number states tend to be more complex than in the chromothriptic. Monte Carlo simulations were used to generate a progressive evolution model with sequential accumulation of observed rearrangements (n=100 simulations per number of SVs). mPDAC S821 showed fewer copy number states on chr4 than expected in the progressive model. Mean is indicated as a black point and lines represent the 95% CI. **s**, Chromothriptic tumors typically feature interspersed loss and retention of heterozygosity. Accordingly, there was a high overlap between deleted regions and LOH segments on chr4 (Jaccard index (J) = 0.99). **t**, In a chromothriptic model, DNA shattering typically occurs on a single haplotype. M-FISH showed that significant loss of chromosomal content occurred on only one copy of chr4. **u**, To show random chromothriptic DNA shattering and re-joining, observed segments (n=73) were re-ordered by running Monte Carlo simulations ($n=10^3$) that generate a background probability distribution. S821 segment order lies within the chromothriptic null model. Two-sided P=0.78. **v**, All 4 SV-types are uniformly distributed in a chromothriptic tumor model. P=0.43; χ_-goodness-of-fit test. **w**, In a chromothriptic model, paired end connection types (as given by the SV-type) induce an alternating sequence of DNA segment ends when ordered according to the genomic position on the original chromosome. Tendency towards this alternating 3'-to-5' pattern of rearranged DNA segment ends (n=146) was tested by using right-sided Wald-Wolfowitz runs test. $P<10^{-12}$. **x**, Mutation clusters in relation to breakpoint junctions involved in chromothripsis are shown as rainfall plot for primary PDAC from PK mouse S821. Each dot represents a single somatic nucleotide variation (SNV) and is ordered on the x-axis according to its position in the

mouse genome. The distance of each SNV to the previous SNV in the genome is shown on the y-axis. The coloring of individual SNV dots indicates the type of nucleotide substitution. **y**, Chr4 “zoom-in” from (x). Breakpoint junctions are shown according to their genomic position on chr4. No mutation clusters - neither in absence nor in combination with breakpoint junctions - were detected, consistent with chromothripsis involving end joining DNA repair mechanisms. This is in contrast to other complex rearrangement types, such as chromoanasynthesis, which arise through replication-based mechanisms with breakpoint-associated high mutation rates (e.g. kataegis).

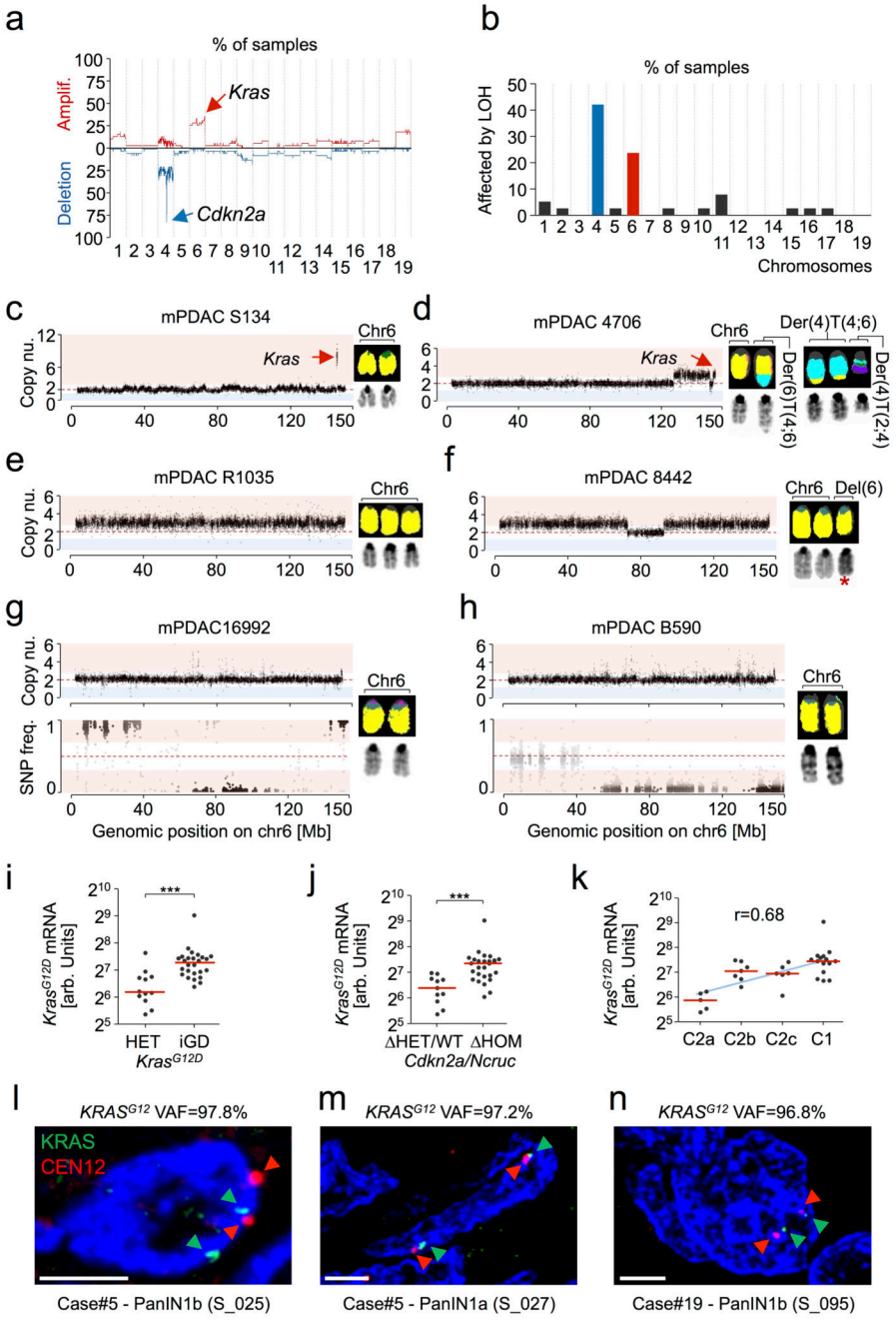

Extended Data Figure 3. Specificity, timing, mechanisms and impact of *Kras*^{G12D} gene dosage alterations on gene expression in pancreatic tumorigenesis.

a, Overlay of copy number profiles of primary mPDAC cell cultures from PK mice (n=38) as determined by aCGH. Y-axis shows frequency of a genomic region to be amplified (up) or deleted (down) in the cohort, with *Cdkn2a* and *Kras* loci being most frequently affected by CNAs. **b**, Prevalence of LOH in primary mPDAC cell cultures from PK mice (n=38) based on whole exome sequencing (WES) data. A chromosome was considered to be affected by LOH if the SNP frequency was shifted to ≤0.1 or ≥0.9 in a segment with a size ≥200kb.

LOH on chr4 is frequently the consequence of heterozygous deletions involving the *Cdkn2a* locus. By contrast, LOH on chr6 is predominantly copy number neutral and linked to increase in $Kras^{G12D}$ gene dosage. Chr4 (home of *Cdkn2a*) and chr6 (home of *Kras*) show markedly increased rates of LOH as compared to all other chromosomes reflecting their functional importance during tumorigenesis. **c-h**, Genetic mechanisms of $Kras^{G12D}$ gene dosage alterations as identified by aCGH, M-FISH and whole exome sequencing (WES) in pancreatic cancers from PK mice. The observed types of increased $Kras^{G12D}$ gene dosage acquisition were: **(i)** focal gain (affecting ≤50% of the chromosome length), arising either through replication-based mechanisms (2 cases, one with high-level $Kras^{G12D}$ amplification [shown in c] and one with low level amplification) or translocation and subsequent amplification of the translocated chromosome (one case [shown in d]), **(ii)** arm-level gain (affecting ≥50% of the chromosome length) arising through mitotic errors (7 cases of whole-chromosome gain [example shown in e], occasionally [2 cases] with concomitant intra-chromosomal deletions or translocations not affecting *Kras* [example shown in f]) and (iii) copy-number neutral LOH (CN-LOH, $Kras^{G12D}$ homozygosity, acquired uniparental disomy), arising either through mitotic recombination (affecting parts of chr6 [shown in h]) or chromosomal missegregation (duplication of $Kras^{G12D}$-mutant chr6 and loss of wild-type chr6 [shown in g]). **c**, mPDAC S134 shows a high-order focal amplification of $Kras^{G12D}$. Sharp borders, small size of the amplification (600kb) and strong increase in copy number (4x) indicate that $Kras^{G12D}$ was amplified through multiple cycles of repeated template-switching by a replication-based DNA repair mechanism. $Kras^{G12D}$ mutant allele frequency is 89.1%. **d**, Tumor 4706 carries a focal amplification of $Kras^{G12D}$. M-FISH analysis revealed that the mutant $Kras^{G12D}$ allele (chr6) was likely first affected by a reciprocal translocation of chr4 and chr6, resulting in two rearranged chromosomes: Der(4)T(4;6) and Der(6)T(4;6). Subsequently, Der(4)T(4;6) was missegregated through mitotic error resulting in focal gain of the $Kras^{G12D}$ locus. $Kras^{G12D}$ mutant allele frequency is 72.2%. **e**, mPDAC R1035 shows 'classical' whole chromosome gain (trisomy) of chr6, which was likely generated through mitotic error/missegregation. The $Kras^{G12D}$ mutant allele frequency is 69.8%. **f**, In tumor 8442 arm-level gain of $Kras^{G12D}$ was likely generated through mitotic missegregation of chr6. Intra-chromosomal deletion on one of three chromosomes (19.6Mb) does not affect *Kras*. $Kras^{G12D}$ mutant allele frequency is 66.4%. Asterisk, chr6 with reduced length resulting from intra-chromosomal deletion. **g-h**, mPDAC 16992 and B590 display copy-number neutral LOH (CN-LOH) leading to increased $Kras^{G12D}$ gene dosage. $Kras^{G12D}$ mutant allele frequency is 99.2% and 96.3%, respectively. The SNP pattern of chr6 in mPDAC 16992 reveals that the whole chromosome is affected by CN-LOH indicating chromosome missegregation (duplication of the $Kras^{G12D}$-mutant chr6 and loss of wild-type chr6) as the underlying mechanism. By contrast, in mPDAC B590 only a partial region of chr6 is affected by CN-LOH, therefore probably resulting from mitotic recombination. **i**, Allele-specific $Kras^{G12D}$ mRNA expression in $Kras^{G12D\text{-}HET}$ (n=12) vs. $Kras^{G12D\text{-}iGD}$ (n=26) primary PDAC cell cultures from PK mice as detected by combined analysis of amplicon-based RNA-Seq (proportion of mutant/wild-type *Kras* mRNA) and 3'-prime pA RNA-Seq (amount of total *Kras* mRNA, but not the proportion of mutant/wild-type *Kras* mRNA due to sequencing of 3'-prime transcript ends; see Methods section). This figure is related to Fig. 2b. ***P≤0.001, two-tailed Mann-Whitney test; bars, median. **j**, Mutant $Kras^{G12D}$ mRNA levels in $Cdkn2a/Ncruc^{\Delta HET/WT}$ (n=11) vs. $Ckdn2a/Ncruc^{\Delta HOM}$

(n=27) primary PDAC cell cultures from PK mice as detected by combined amplicon-based RNA-Seq and 3'-prime pA RNA-Seq. This figure is related to Extended Data Figure 5f. ***P≤0.001, two-tailed Mann-Whitney test; bars, median. **k**, Mutant $Kras^{G12D}$ mRNA levels in transcriptional clusters of mPDAC from PK mice (C2a/b/c/C1, n=5/7/6/15) as detected by combined amplicon-based RNA-Seq and 3'-prime pA RNA-Seq. This figure is related to Fig. 5d. $P=1.6*10^{-5}$, two-sided Pearson correlation; bars, median. **l-n**, Interphase fluorescence in situ hybridization (FISH) for the analysis of copy-number and ploidy states at the *KRAS* locus on chr12 in human pancreatic intra-epithelial neoplasia (PanIN) with $KRAS^{G12}$ variant allele frequencies (VAFs) of ~100%. $KRAS^{G12}$ VAFs are indicated above each FISH profile as detected by amplicon-based deep sequencing. A VAF of ~100% can be caused either by loss of the wild-type *KRAS*-locus (hemizygosity of $KRAS^{G12\text{-}MUT}$: one $KRAS^{G12\text{-}MUT}$ allele per cell) or by CN-LOH (acquired uniparental disomy; homozygosity of $KRAS^{G12\text{-}MUT}$: two $KRAS^{G12\text{-}MUT}$ alleles per cell). All samples show a diploid genome as suggested by CEN12 (two red signals per nucleus). Neither loss of one *KRAS* allele nor monosomy of chr12 was observed providing evidence for CN-LOH and increased $KRAS^{G12\text{-}MUT}$ gene dosage in hPanIN. Scale bars, 2.5μm; CEN12, centromere probe chr12.

Europe PMC Funders Author Manuscripts

Europe PMC Funders Author Manuscripts

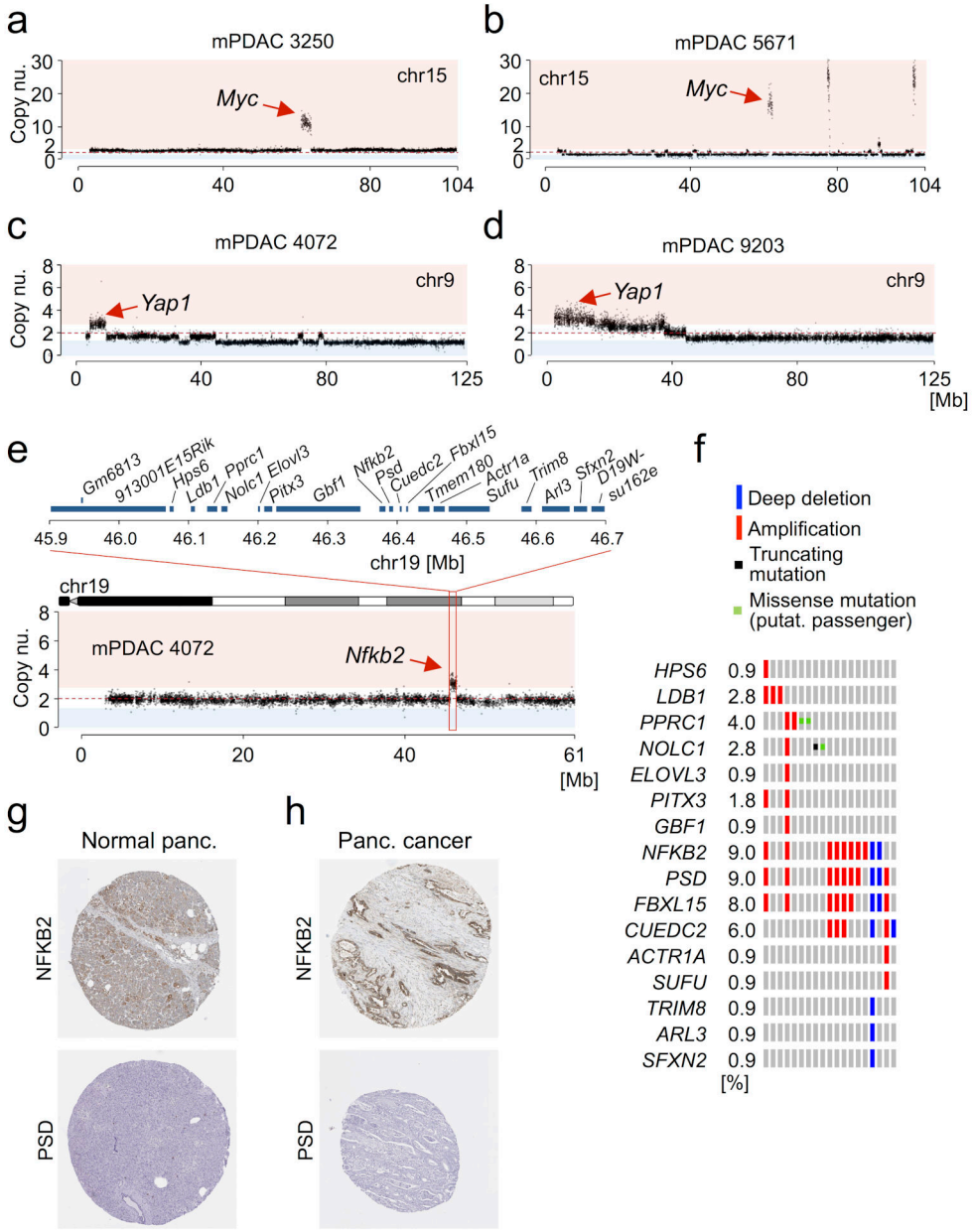

Extended Data Figure 4. Enrichment for amplification of alternative oncogenic drivers in mPDACs of PK mice with *Kras*$^{G12D\text{-}HET}$ status.

a-b, Two primary mPDACs with strong focal *Myc* amplification on chr15 are shown, as detected by aCGH. Red dashed line indicates no copy number change. **c-d**, Focal copy number gains targeting the *Yap1* locus on chr9 in primary mPDACs 4072 and 9203 as revealed by aCGH. **e**, Chr19 was also frequently subject to arm-level gain (see Fig. 1c and Extended Data Figure 1l). Primary mPDAC of PK mouse 4072 harbors a focal gain on chr19 containing 20 genes: *9130011E15Rik*, *Gm6813*, *Hps6*, *Ldb1*, *Pprc1*, *Nolc1*, *Elovl3*, *Pitx3*,

Gbf1, *Nfkb2*, *Psd*, *Fbxl15*, *Cuedc2*, *Tmem180*, *Actr1a*, *Sufu*, *Trim8*, *Arl3*, *Sfxn2*, *D19Wsu162e*. **f**, Cross-species analyses revealed that the orthologous region on human chr10 is also subject to recurrent amplifications in human PDAC (8 out of 109 hPDACs have focal amplifications; data from Witkiewicz *et al.*6). Of the 20 mouse genes, sixteen could be assigned to orthologues in humans. Further analyses revealed that only two genes, *NFKB2* and *PSD*, are within the minimal overlapping region of recurrent amplification (data from6 and oncoplot from cBioPortal60,61). **g**, *NFKB2*, but not *PSD*, shows medium protein expression in exocrine glandular cells of normal pancreatic tissue, as detected by immunohistochemistry (IHC, data from TheHumanProteinAtlas62). **h**, *NFKB2* is highly expressed in 17% (2/12) of stained hPDAC biopsies as shown by IHC. In contrast, there was no *PSD* expression in any of the analyzed pancreatic cancers (0/12). Protein expression data was used from TheHumanProteinAtlas62.

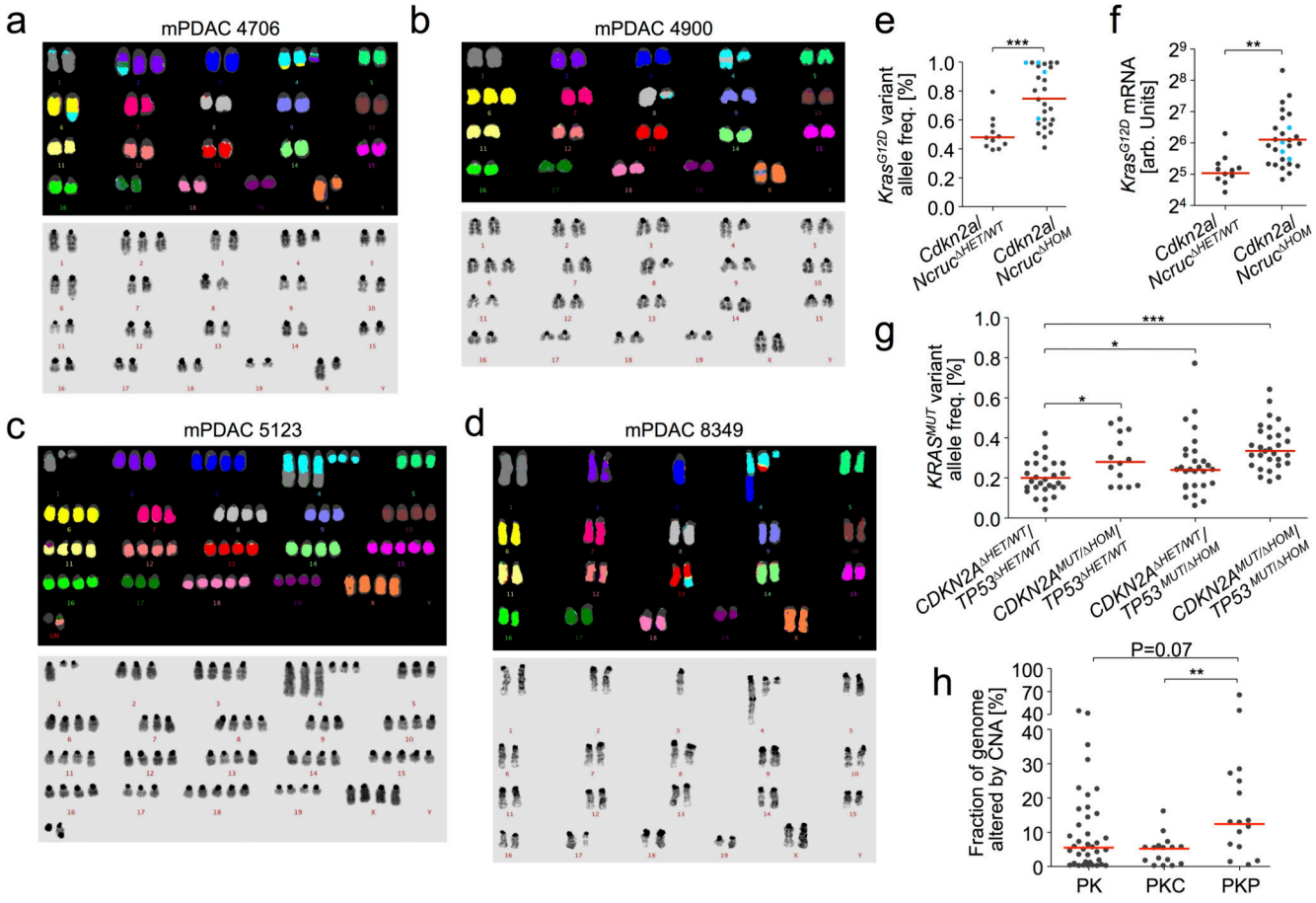

Extended Data Figure 5. Characterization of *Cdkn2a* (chr4) alterations and correlation with *Kras*^{MUT} gene dosage variation and mRNA expression in mouse and human PDAC.

a-d, *Cdkn2a* alteration on mouse chr4 can occur through arm-level, complex or focal loss as well as uniparental disomy (see Figure 3). In addition, chr4 is frequently involved in inter-chromosomal translocations. Examples of representative karyotypes of primary pancreatic cancer cultures derived from PK mice with translocations involving chr4, likely affecting the *Cdkn2a* locus. In all 4 cases, chr4 translocations were found in all 10 metaphase spreads of

each cancer, indicating their early acquisition during tumor evolution. **a**, mPDAC 4706 with diploid karyotype: 42, XX, del(X), +2, der(2)t(2;4)is(2;4), der(4)t(4;6)*2, +der(4)t(2;4), der(6)t(4;6). **b**, mPDAC 4900 also features a diploid karyotype: 41, XX, der(X)is(X;4), der(4)is(4;8), del(4), +6, der(8)t(4;8). **c**, mPDAC 5123 underwent polyploidization, after translocation of chr4 with chr1 and an deletion on the other copy: 78, XXXX, -1, del(1)*2, -2, +4*2, der(4)t(1;4)*3, del(4)*3, -5, -7, -9, +15, -17, +18 **d**, mPDAC 8349 shows a diploid karyotype: 40,XX, der(4)t(3;4), der(4)t(4;13), +del(4), der(13)t(4;13). **e**, $Kras^{G12D}$ variant allele frequencies detected by amplicon-based deep sequencing of the *Kras* locus are higher in $Cdkn2a/Ncruc^{\Delta HOM}$ mPDAC (n=27) as compared to $Cdkn2a/Ncruc^{\Delta HET/WT}$ (n=11) pancreatic cancers. All cancers are from PK mice. Blue dots indicate tumors with complete *Ncruc* deletion. ***P≤0.001, two-tailed Mann-Whitney test; bars, median. **f**, Allele-specific expression of mutant $Kras^{G12D}$ mRNA is increased in primary tumors from PK mice with $Cdkn2a/Ncruc^{\Delta HOM}$ (n=27) background in comparison to $Cdkn2a/Ncruc^{\Delta HET/WT}$ (n=11) cancers. Primary mPDACs with homozygous loss of *Ncruc* are highlighted in blue. $Kras^{G12D}$ expression was analyzed by combining amplicon-based RNA-Seq and qRT-PCR (as described in the Methods section). **P=0.003, two-tailed Mann-Whitney test; bars, median. **g**, $KRAS^{MUT}$ variant allele frequencies based on WES in a published dataset of microdissected human PDAC (Witkiewicz *et al.*, reduced stromal content) was analyzed with respect to *CDKN2A* and *TP53* status. $KRAS^{MUT}$ allele frequency was higher in mutated/homozygous deleted *CDKN2A* and/or *TP53* ($CDKN2A^{MUT/\Delta HOM}$/$TP53^{MUT/\Delta HOM}$; hPDACs as compared to cancers with $CDKN2A^{\Delta HET/WT}$/$TP53^{\Delta HET/WT}$ status (from left: n=28, n=14, n=28, n=30). Two-sided rank-based ANOVA ($P=5.8*10^{-6}$); post hoc testing with two-sided Tukey honest significant difference test, *adj. P≤0.05, ***adj. P≤0.001; bars, median. **h**, Fraction of the genome altered by copy number changes detected by aCGH in primary mPDACs of PK (n=38), PKC (n=16) and PKP (n=16) mice. PKP mice show a significantly increased CNA load as compared to PKC mice. Two-sided rank-based ANOVA (P=0.01); post hoc testing with two-sided Tukey honest significant difference test, **adj. P=0.009, adj. P-values for group wise comparisons are shown; bars, median. Del, deletion; der, derivative chromosome; is, insertion; t, translocation; „-“, chromosome loss; „+“, chromosome gain.

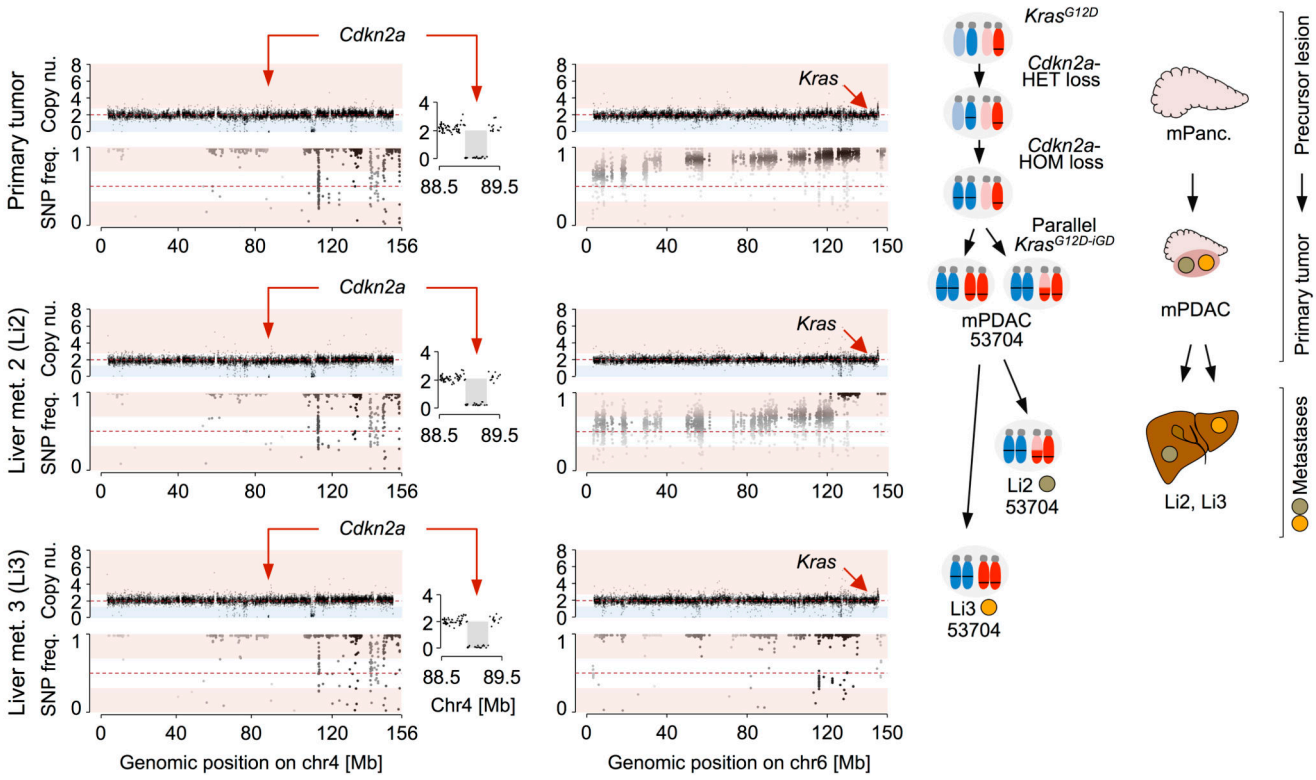

Extended Data Figure 6. Complete *Cdkn2a* barrier loss precedes *Kras*$^{G12D\text{-}iGD}$ in primary mPDAC of PK mouse 53704.

Copy number alterations at chr4 (*Cdkn2a*) and chr6 (*Kras*) in mPDAC 53704 and corresponding metastases, as detected by aCGH (top) and whole-exome sequencing based SNP pattern analysis (bottom). The primary cancer and both liver metastases display identical focal deletions of *Cdkn2a* and similar SNP patterns on chr4 revealing that all lesions share the same ancestor cell with complete *Cdkn2a* loss. By contrast, SNP analysis on chr6 revealed discordant patterns in the primary mPDAC and both metastases. Li2 shows partial LOH of a distal region on chr6 involving the *Kras* locus, while LOH in Li3 involves the whole chr6. This explains the step-wise LOH pattern observed on chr6 in the primary mPDAC. The graphic on the right shows the combined interpretation of CNV/LOH profiles, which suggests the following sequence of genetic events during tumor evolution: The initial *Kras*^{G12D} mutation was followed by focal deletion of one copy of *Cdkn2a*. In a subsequent genetic event, the second copy of *Cdkn2a* was lost by chr4 missegregation and copy-number neutral LOH. Complete barrier loss allowed for convergent evolution of increased *Kras*^{G12D} gene dosage through copy-number neutral LOH and gave rise to independent metastases in the liver. *Note*: A major obstacle for equivalent human studies is the limited availability of human matched primary/metastases samples, particularly of treatment naive ones. We performed cross-species analyses using data from a recent study, which analyzed human treatment-naive metastatic PDACs by whole-genome sequencing8 and provided *CDKN2A* and *KRAS* copy number data for matched primaries/metastases from 3 patients. In one patient the sequential order of *CDKN2A* deletion and *KRAS* amplification could be reconstructed: homozygous *CDKN2A* deletions were identical in all primaries and

Europe PMC Funders Author Manuscripts

metastases, whereas there were 5 different *KRAS* gains in the 6 metastases. This suggests convergent evolution of mutant *KRAS* gene dosage gain upon homozygous *CDKN2A* loss in this patient, in line with similar data in large series of mouse cancers and their metastases (see Figure 3e).

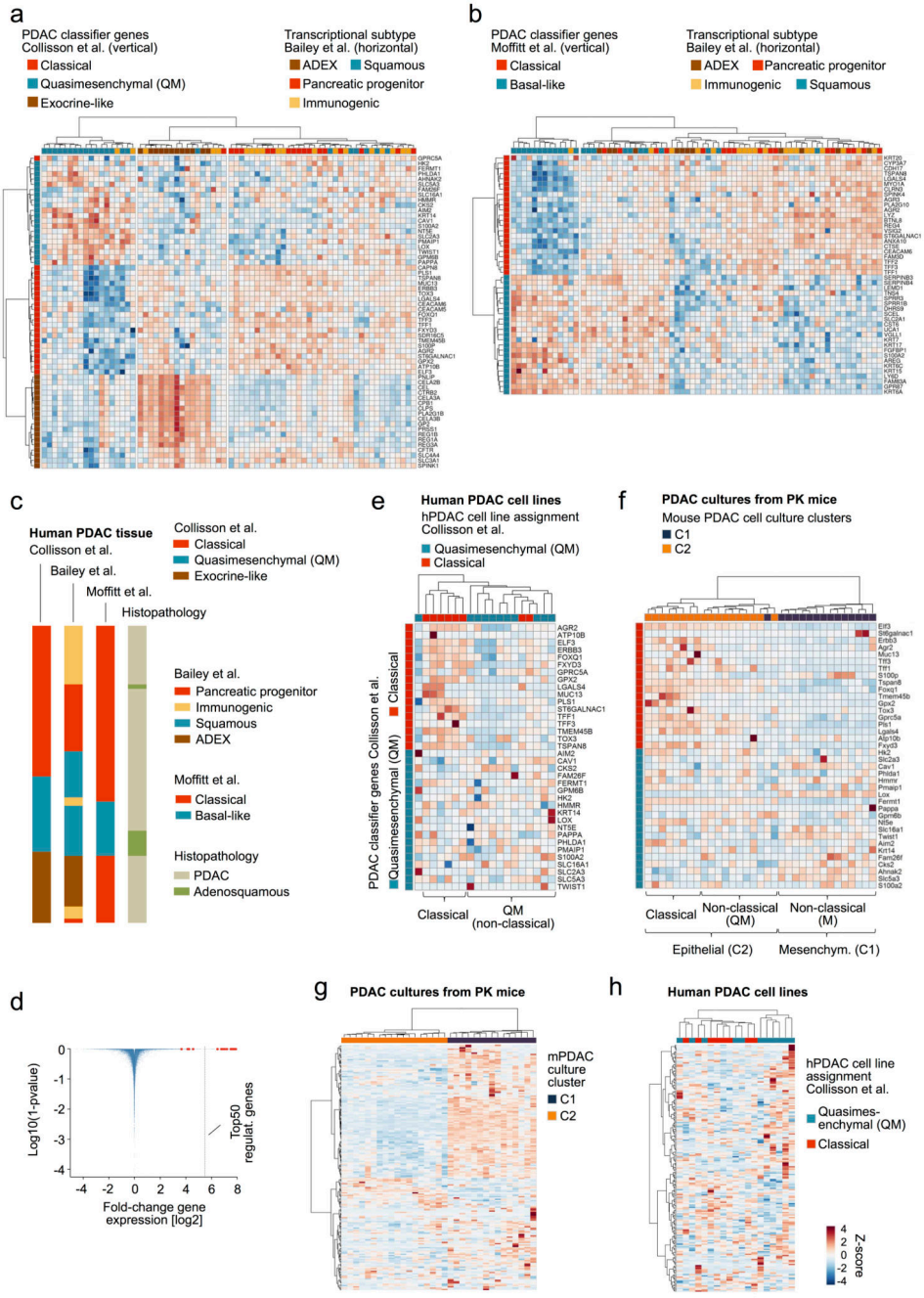

Extended Data Figure 7. Transcriptome-based subtyping of human primary pancreatic cancer and classification of human PDAC cell lines and primary PDAC cell cultures from PK mice.

a-c, Independent cross-comparison of transcriptional classification systems from Collisson *et al.*28, Moffitt *et al.*29 and Bailey *et al.*7. Collisson *et al.* performed PDAC microdissection

and defined 3 transcriptional subtypes: classical, quasimesenchymal (QM) and exocrine-like. Moffitt *et al.* defined 2 subtypes (classical, basal-like) using (i) virtual separation of tumor and non-tumor gene expression patterns, (ii) transplantation studies and (iii) human PDAC cell lines; and proposed that the exocrine-like signature stems from exocrine pancreatic cells, rather than from the cancer cells. Bailey *et al.* used bulk tumors and defined 4 subtypes (pancreatic progenitor, immunogenic, squamous, aberrantly differentiated endocrine exocrine [ADEX]). RNA-Seq data from PDAC and adenosquamous pancreatic carcinoma from Bailey *et al.* was used for cross-comparison of classification systems. Other histological subentities of pancreatic cancer were excluded (e.g. IPMN, MCN, acinar cell carcinoma). The Bailey subtyping for this dataset was available. **a**, Unbiased hierarchical clustering of primary pancreatic cancer samples (n=71) from Bailey *et al.* using Collisson classifier genes. **b**, Subtyping of primary pancreatic cancer samples (n=71) from Bailey *et al.* using classifier genes defined by Moffitt *et al.* **c**, Consensus clustering based on analyses performed in a/b. There is considerable overlap between at least two subtypes, which are in large parts captured by the initially proposed Collisson classical and quasimesenchymal (QM) signatures (which are also detected in mouse and human PDAC cell lines; see Extended Data Figure 7e-h). The Bailey classification (based on bulk tissue analyses) suggests that Collisson classical cancers (microdissected cancer tissue) can be further sub-stratified in some with and some without a strong immune cell infiltration. The Moffitt classification suggests that the Collisson exocrine-like signature (Bailey ADEX subtype) stems from “contaminating” healthy exocrine pancreatic cells, based on the evidence described above. Given that the Collisson exocrine-like signature was derived from microdissected PDAC, such “contamination” is only conceivable, if exocrine-like signature genes were dramatically higher expressed in pancreatic acinar cells as compared to PDAC cells. **d**, Volcano plot showing strongly upregulated expression of exocrine-like genes in human wild-type pancreas (13 to 241 fold; median: 183-fold upregulation). Note that 15 out of 19 exocrine-like signature genes (red dots) are among the top50 genes upregulated in human wild-type pancreas (n=3) as compared to hPDAC cell lines (n=30) (y axis is calculated on Benjamini-Hochberg adj. P-values derived from R package limma [see Methods section]). Although these data do not exclude the existence of exocrine-like PDACs, they support the possibility that “contamination” with few acinar cells can impose an exocrine-like signature on a cancer. This might explain why human or mouse PDAC cell lines don´t cluster into the exocrine-like subtype (see also Extended Data Figure 7e-f below). **e**, Hierarchical clustering of microarray-based expression profiles using Collisson identifier genes28 on human PDAC cell lines (n=19, GEO series GSE17891). As also described earlier by Collisson *et al.*, only two subtypes can be detected in human cell line collections: classical and quasimesenchymal (QM). Of note, the most prominent change in the QM cell lines is downregulation (extinction) of the classical assigner genes, whereas expression of QM classifier genes is quite variable. We therefore also use here the terms classical and non-classical. **f**, Projection of the Collisson classifiers on mouse PDAC cell culture transcriptomes (n=33) also identified classical and non-classical subtypes. The non-classical subtype contained a subset of mPDAC cell cultures from cluster C2a/b/c (epithelial morphology; equivalent of human QM) and all cluster C1 mPDACs (mesenchymal morphology; “M” cluster). **g**, Application of a human EMT hallmark gene set52 for hierarchical clustering of expression profiles from primary PDAC cultures (PK mice; n=33)

resulted in a separation of C1 (mesenchymal) and C2a/b/c (epithelial) cell lines. **h**, Projection of the EMT hallmark gene set on human PDAC cell line transcriptomes (n=19, GEO series GSE17891) did not result in a clear separation of samples, indicating underrepresentation of the mesenchymal M subtype (equivalent to murine C1/“M”) in available human cell line collections. As shown in Extended Data Figure 9b, however, the EMT signature is detectable in undifferentiated human pancreatic carcinoma, which is the human equivalent of the mesenchymal mouse PDACs in C1.

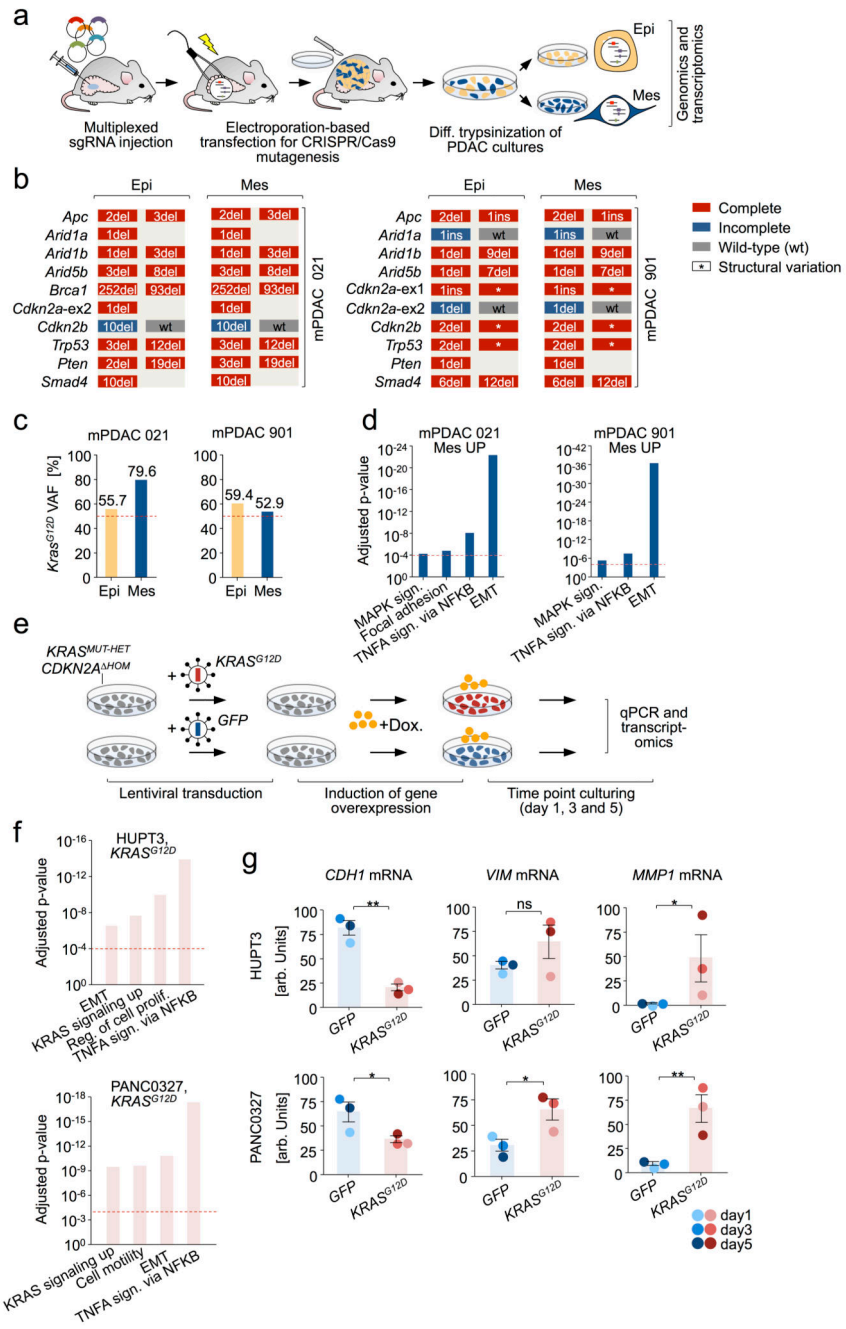

Europe PMC Funders Author Manuscripts

Extended Data Figure 8. Functional analyses to study the role of *Kras*^{G12D} gene dosage increase in EMT. a-d, Multiplexed somatic CRISPR/Cas9 mutagenesis for phylogenetic tracking of epithelial/mesenchymal mPDAC clones *in vivo*.

a, Graphic demonstrates major steps of multiplexed gene editing by pooled delivery of CRISPR/Cas9 vectors, each targeting a different tumor suppressor gene in the pancreas of PK mice. Electroporation-based transfection enables low-frequency mosaic vector delivery (average of 120 cells per pancreas are transfected) to induce clonal tumors. Primary tumor cell cultures were screened for the simultaneous presence of epithelial and mesenchymal cells. Two such cancers were identified (mPDACs from mouse 021 and mouse 901) and subjected to differential trypsinization in order to enrich for each morphology. **b**, Amplicon-based deep sequencing of all sgRNA-targeted loci revealed identical indel patterns in both epithelial/mesenchymal culture pairs. This shows (i) that epithelial and mesenchymal cells originate from the same clone and (ii) that the CRISPR-induced mutations are not contributing to the differential phenotype. **c**, *Kras*^{G12D} variant allele frequencies in epithelial and mesenchymal cell cultures from mPDAC 021 and mPDAC 901, as detected by amplicon-based deep sequencing. Both cancers had increased *Kras*^{G12D} expression in mesenchymal cells (see Fig. 5e). In mPDAC 021 this is due to selective amplification of the *Kras*^{G12D} allele in mesenchymal cells. In mPDAC 901 genetic *Kras*^{G12D} amplification was not observed, suggesting induction of increased *Kras* expression in mesenchymal cells by other mechanisms. **d**, Gene set enrichment analysis using “Molecular Signatures Database” (MSigDB) of differentially regulated genes in mesenchymal versus epithelial mPDACs based on RNA-Seq. Mesenchymal clones of mPDAC 021 and mPDAC 901 show an upregulation of genes involved in “MAPK signaling pathway” and “EMT” as compared to the corresponding epithelial clones, in line with increased *Kras*^{G12D} gene dosage (a full list of enriched gene sets is provided for comparisons in Supplementary Table 15). FDR-adjusted P-values are shown on y axis. Representative data from one experiment are shown. **e-g,** induction of EMT-like transcriptional programs by *KRAS*^{G12D} overexpression in human PDAC cell lines. **e**, Graphic of experimental workflow. Two human PDAC cell lines (HUPT3 and PANC0327) with homozygous *CKDN2A* loss (*CDKN2A*$^{\Delta HOM}$) and heterozygous *KRAS*^{MUT} (*KRAS*$^{MUT\text{-}HET}$) status were transduced with lentivirus carrying doxycycline-inducible *KRAS*^{G12D} or GFP-control expression constructs. *KRAS*^{G12D} or GFP expression was induced by adding doxycycline for 1, 3 and 5 days. **f**, Gene set enrichment analysis using “Molecular Signatures Database” (MSigDB) of differentially regulated genes in *KRAS*^{G12D}- versus GFP-induced hPDAC cell lines HUPT3 and PANC0327 based on RNA-Seq. Upon doxycycline treatment, both hPDAC cell lines showed a consistent upregulation of genes involved in “KRAS signaling up” and “EMT” (a full list of enriched gene sets is provided for both cell lines in Supplementary Table 16). FDR-adjusted P-values are shown on y axis. **g**, Expression of marker genes for epithelial (*CDH1*) or mesenchymal (*VIM*) cell differentiation and invasion/matrix disassembly (*MMP1*) was validated by qPCR (normalized to *GAPDH* and *PPIA*). In line with RNA-Seq data *KRAS*^{G12D}-induced cells show an increased expression of the mesenchymal marker gene *VIM*, increased expression of *MMP1* and reduced levels of epithelial marker gene *CDH1*. *P≤0.05, **P≤0.005, ns=not significant, two-tailed t-test; bars=mean; error bars=SEM.

Europe PMC Funders Author Manuscripts

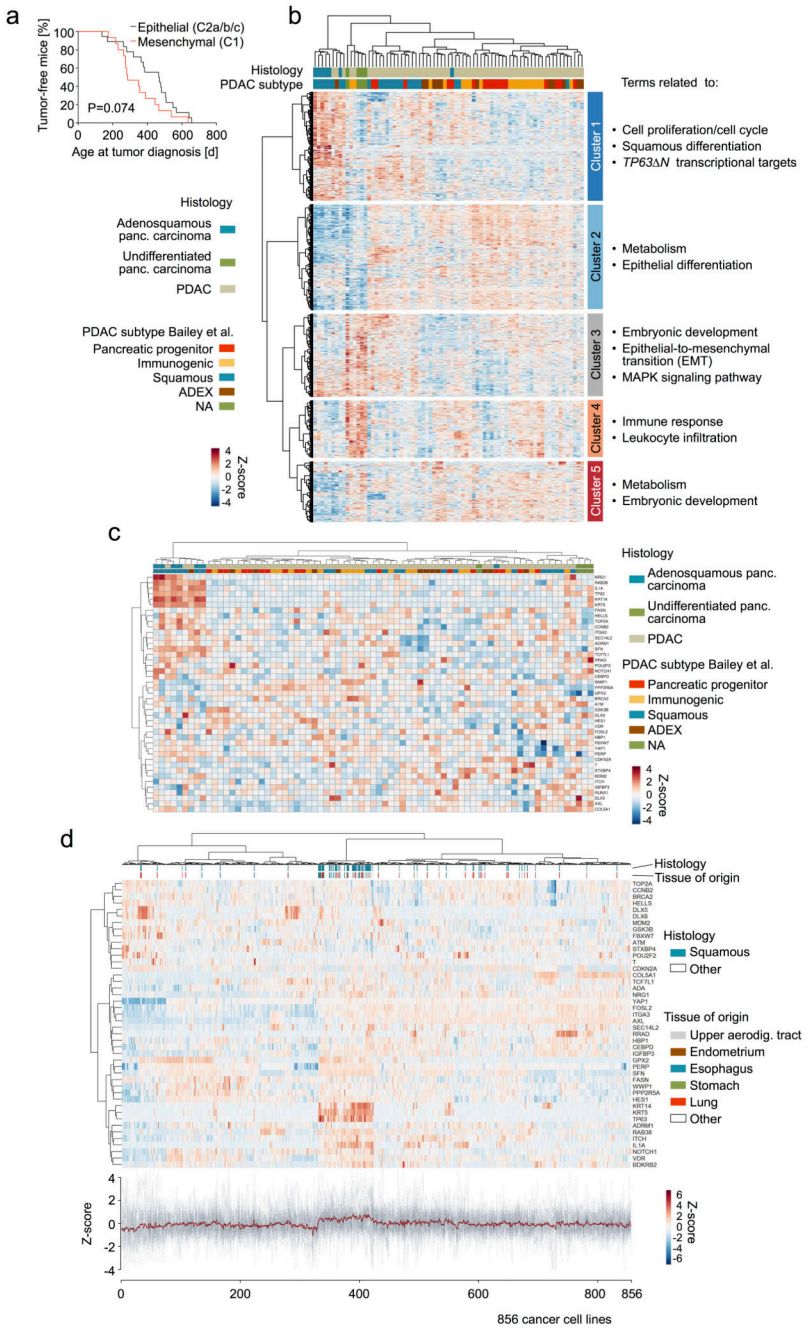

Extended Data Figure 9. Transcriptional profiles of human undifferentiated pancreatic carcinomas are enriched for signatures of oncogenic signaling intensification and EMT but not for activation of *TP63ΔN* transcriptional network.

a, Primary pancreatic tumors from PK mice with a mesenchymal phenotype (C1 cluster, n=15) are almost exclusively classified as undifferentiated/sarcomatoid by histopathological evaluation and tend to have a reduced age at diagnosis when compared to epithelial (C2a/b/c cluster, n=18) tumors (histopathological grade 1 to 3 [G1-G3]). This aggressive behavior of undifferentiated pancreatic carcinoma is also observed in human patients and is associated with worse clinical outcome33. P-value calculated by two-sided log-rank test. **b**,

Comparison of publically available expression profiles of human undifferentiated pancreatic carcinoma (n=4), PDAC (WHO grade 1 to 3 [G1-G3], n=64) and adenosquamous pancreatic carcinoma (n=7). Human samples with the above histopathological characteristics for which expression-based subtype information from Bailey *et al.*7 was available were used and complemented with available undifferentiated pancreatic carcinomas from the ICGC PACA-AU cohort (Supplementary Table 18). Other histological subentities of pancreatic cancer were excluded (e.g. IPMN, MCN, acinar cell carcinoma). ANOVA was performed to select genes which are differentially expressed in at least one of the six defined subgroups of pancreatic cancer: **(i)** undifferentiated, **(ii)** adenosquamous pancreatic carcinoma and (iii-vi) PDAC (G1-G3) sub-stratified in pancreatic progenitor, immunogenic, squamous and aberrantly differentiated endocrine exocrine (ADEX) Bailey subtypes. Differentially regulated genes were used for unbiased hierarchical clustering of these pancreatic cancer transcriptional profiles. Five sub-clusters of co-regulated gene expression could be identified according to the cluster tree on the y-axis (separated by white horizontal bars in the heatmap). Gene set enrichment analysis using “Molecular Signatures Database” (MSigDB) was performed for individual sub-clusters and terms related to predominating gene sets/ pathways are annotated for each cluster on the right (full list provided in Supplementary Table 17). Undifferentiated pancreatic carcinomas cluster together and are associated with (i) upregulation of genes in cluster 3 (containing MAPK signaling pathway and gene sets relevant during embryonic development or EMT) and (ii) downregulation of genes in clusters 2 and 5, which contain gene sets related to epithelial cell differentiation, embryonic development or metabolic signatures. This reflects the pathway enrichment signature in the equivalent undifferentiated (mesenchymal) mouse PDACs (cluster C1/"M" in PK mice; see Extended Data Figure 7g) and provides further support for the link between *KRAS* signaling intensification, EMT and the undifferentiated tumor phenotype. The immunogenic PDAC subtype showed high expression of cluster 4 genes, which was also strong (even elevated) in undifferentiated pancreatic carcinomas, suggesting an increased immune cell infiltration in undifferentiated carcinomas. Cluster 1 contained gene sets related to cell proliferation/cell cycle, squamous differentiation and *TP63ΔN* transcriptional targets, which were most highly overexpressed in pancreatic carcinomas with adenosquamous histology. Undifferentiated pancreatic carcinomas did not show activation of the *TP63ΔN* transcriptional targets. This suggests that activation of *TP63ΔN* transcriptional targets is not causally linked to *KRAS* signaling intensification and EMT (see also Extended Data Figure 9c-d, showing a lack of association of undifferentiated carcinomas with *TP63ΔN* transcriptional network activation). **c**, Unbiased hierarchical clustering of human pancreatic carcinomas with adenosquamous histology (n=7) as well as PDACs (WHO grade 1 to 3 [G1-G3], n=64) and undifferentiated pancreatic carcinomas (n=4) (sample set as in Extended Data Figure 9b) using a list of validated *TP63ΔN* transcriptional targets53. Pancreatic cancers with adenosquamous differentiation were significantly enriched in a cluster showing increased *TP63ΔN* transcriptional network activity (P≤0.001, two-sided Fisher’s exact test, OR 130, 95% CI 11.6-1452). Undifferentiated pancreatic carcinomas did not contribute to this cluster. In line, pancreatic cancers from PK mice did not show differential regulation of the *TP63ΔN* network, reflecting the lack of adenosquamous tumors in this cohort (not shown). **d**, Unbiased hierarchical clustering across solid cancers (Cancer Cell Line Encyclopedia, n=856) using the same gene list showed a strong enrichment of tumors with squamous

differentiation in the sub-cluster with highest *TP63ΔN* transcriptional network expression (P≤0.001, two-sided Fisher's exact test, OR 28.1, 95% CI 16.4-48.1), in line with the observation of Hoadley *et al.*63 that *TP63ΔN* is a signature for squamous differentiation across cancers.

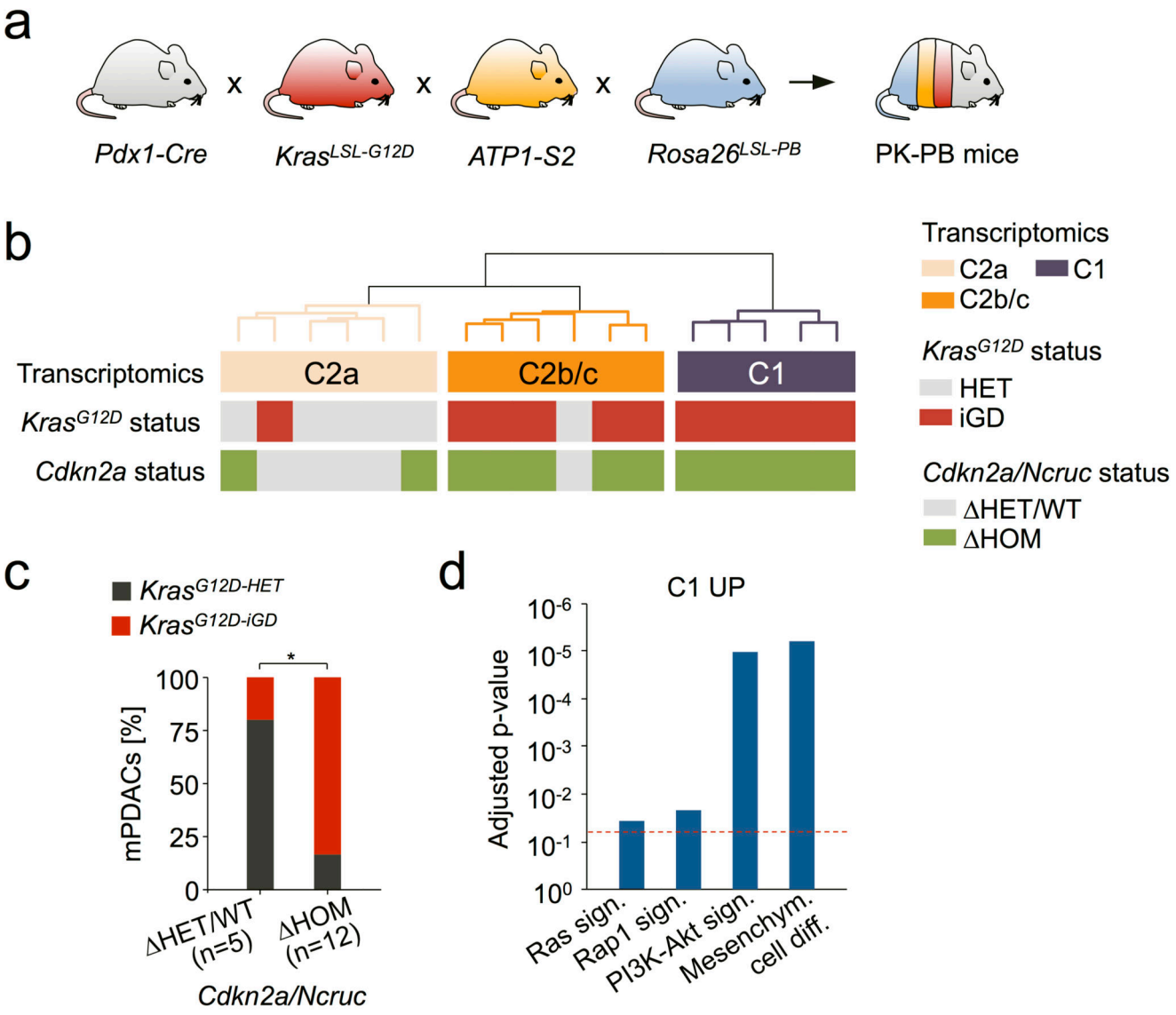

Extended Data Figure 10. *Kras*^{G12D}-gene dosage is a critical determinant of PDAC biology in a mouse model with high mutational load.

The mutational burden in primary PDAC cultures of PK mice was significantly lower as compared to human PDAC studies (see Fig. 1b). To account for this potential confounding factor and to test if our discoveries in PK mice also apply in a setting of high mutational burden, we used a mouse model combining *Kras*^{G12D} mutation and *PiggyBac* transposon-based insertional mutagenesis (PK-PB mice13). PK-PB mice show accelerated tumorigenesis as compared to PK mice. PK-PB derived tumors had an extensive mutational burden (median of 494 transposon insertions per tumor). Primary cultures of PDAC from

Europe PMC Funders Author Manuscripts

PK-PB mice (n=17) were subjected to comprehensive genetic characterization using aCGH, microarray-based gene expression profiling, quantitative transposon insertion site sequencing (QiSeq) and amplicon-based deep sequencing of the *Kras* locus. **a**, Transcriptome profiles of primary PDAC cultures from PK-PB mice (n=17) were used for unbiased hierarchical clustering that resulted in 2 major clusters (C1 and C2), like in PK mice. $Kras^{G12D}$ gene dosage status (as determined by aCGH and amplicon-based deep sequencing of the *Kras* locus) and *Cdkn2a* status (as determined by aCGH and quantitative transposon insertion site sequencing [QiSeq]) are indicated below the cluster tree for each individual tumor. Similarly to PK mice, cluster C2a was characterized by $Kras^{G12D\text{-}HET}$ and $Cdkn2a/Ncruc^{\Delta HET/WT}$ status, whereas mPDACs in clusters C2b/c and C1 had increased $Kras^{G12D}$ gene dosage ($Kras^{G12D\text{-}iGD}$) and were $Cdkn2a/Ncruc^{\Delta HOM}$. The genetic $Kras^{G12D}$-status was significantly associated with expression clusters (P=0.01, two-sided Fisher's exact test) providing further evidence that expression clusters are associated with $Kras^{G12D}$ gene dosage. **b**, Prevalence of $Kras^{G12D\text{-}iGD}$ in cultures of primary mPDAC (from PK-PB mice) with homozygous (n=12) or heterozygous/wild-type (n=5) *Cdkn2a/Ncruc* status. *P=0.03, two-sided Fisher's exact test, OR 20.0, 95% CI 1.4-287.8. **c**, Gene set enrichment analysis using DAVID of upregulated genes in cluster C1 (n=5) as compared to cluster C2 (n=12) of primary mPDAC cultures from PK-PB mice. As in PK mice, PK-PB tumors in C1 are characterized by upregulation of genes enriched in gene sets describing mesenchymal cell differentiation and revealed a strong enrichment for Ras downstream signaling pathways (full list in Supplementary Table 19). FDR-adjusted P-values are shown on y axis. Overall, these analyses show that the biological principles discovered in the PK model also apply to pancreatic cancers from PK-PB mice with high mutational load.

Supplementary Material

Refer to Web version on PubMed Central for supplementary material.

Acknowledgements

We thank the comparative experimental pathology team for valuable discussions and Aaron Selmeier, Laura Dajka, Olga Seelbach, Petra Meyer, Tatjana Schmidt, Julia Eichinger and Teresa Stauber for excellent technical assistance as well as Maximilian Reichert for vector constructs. The work was supported by the German Cancer Consortium Joint Funding Program, the Helmholtz Gemeinschaft (PCCC Consortium), the German Research Foundation (SFB1243; A13/A14) and the European Research Council (ERC CoG No. 648521). The authors declare no competing financial interests.

References

1. Rahib L, et al. Projecting cancer incidence and deaths to 2030: the unexpected burden of thyroid, liver, and pancreas cancers in the United States. Cancer Res. 2014; 74:2913–2921. DOI: 10.1158/0008-5472.CAN-14-0155 [PubMed: 24840647]
2. Jones S, et al. Core signaling pathways in human pancreatic cancers revealed by global genomic analyses. Science. 2008; 321:1801–1806. DOI: 10.1126/science.1164368 [PubMed: 18772397]
3. Campbell PJ, et al. The patterns and dynamics of genomic instability in metastatic pancreatic cancer. Nature. 2010; 467:1109–1113. DOI: 10.1038/nature09460 [PubMed: 20981101]
4. Biankin AV, et al. Pancreatic cancer genomes reveal aberrations in axon guidance pathway genes. Nature. 2012; 491:399–405. DOI: 10.1038/nature11547 [PubMed: 23103869]
5. Waddell N, et al. Whole genomes redefine the mutational landscape of pancreatic cancer. Nature. 2015; 518:495–501. DOI: 10.1038/nature14169 [PubMed: 25719666]

6. Witkiewicz AK, et al. Whole-exome sequencing of pancreatic cancer defines genetic diversity and therapeutic targets. Nat Commun. 2015; 6:6744.doi: 10.1038/ncomms7744 [PubMed: 25855536]
7. Bailey P, et al. Genomic analyses identify molecular subtypes of pancreatic cancer. Nature. 2016; 531:47–52. DOI: 10.1038/nature16965 [PubMed: 26909576]
8. Makohon-Moore AP, et al. Limited heterogeneity of known driver gene mutations among the metastases of individual patients with pancreatic cancer. Nat Genet. 2017; 49:358–366. DOI: 10.1038/ng.3764 [PubMed: 28092682]
9. Jackson EL, et al. Analysis of lung tumor initiation and progression using conditional expression of oncogenic K-ras. Genes Dev. 2001; 15:3243–3248. DOI: 10.1101/gad.943001 [PubMed: 11751630]
10. Schonhuber N, et al. A next-generation dual-recombinase system for time- and host-specific targeting of pancreatic cancer. Nat Med. 2014; 20:1340–1347. DOI: 10.1038/nm.3646 [PubMed: 25326799]
11. Perez-Mancera PA, et al. The deubiquitinase USP9X suppresses pancreatic ductal adenocarcinoma. Nature. 2012; 486:266–270. DOI: 10.1038/nature11114 [PubMed: 22699621]
12. Mann KM, et al. Sleeping Beauty mutagenesis reveals cooperating mutations and pathways in pancreatic adenocarcinoma. Proc Natl Acad Sci U S A. 2012; 109:5934–5941. DOI: 10.1073/pnas.1202490109 [PubMed: 22421440]
13. Rad R, et al. A conditional piggyBac transposition system for genetic screening in mice identifies oncogenic networks in pancreatic cancer. Nat Genet. 2015; 47:47–56. DOI: 10.1038/ng.3164 [PubMed: 25485836]
14. Korbel JO, Campbell PJ. Criteria for inference of chromothripsis in cancer genomes. Cell. 2013; 152:1226–1236. DOI: 10.1016/j.cell.2013.02.023 [PubMed: 23498933]
15. Notta F, et al. A renewed model of pancreatic cancer evolution based on genomic rearrangement patterns. Nature. 2016; 538:378–382. DOI: 10.1038/nature19823 [PubMed: 27732578]
16. Yamada H, et al. Amplifications of both c-Ki-ras with a point mutation and c-myc in a primary pancreatic cancer and its metastatic tumors in lymph nodes. Jpn J Cancer Res. 1986; 77:370–375. [PubMed: 3009377]
17. Heidenblad M, et al. Detailed genomic mapping and expression analyses of 12p amplifications in pancreatic carcinomas reveal a 3.5-Mb target region for amplification. Genes Chromosomes Cancer. 2002; 34:211–223. DOI: 10.1002/gcc.10063 [PubMed: 11979555]
18. Sarkisian CJ, et al. Dose-dependent oncogene-induced senescence in vivo and its evasion during mammary tumorigenesis. Nat Cell Biol. 2007; 9:493–505. DOI: 10.1038/ncb1567 [PubMed: 17450133]
19. Junttila MR, et al. Selective activation of p53-mediated tumour suppression in high-grade tumours. Nature. 2010; 468:567–571. DOI: 10.1038/nature09526 [PubMed: 21107427]
20. Feldser DM, et al. Stage-specific sensitivity to p53 restoration during lung cancer progression. Nature. 2010; 468:572–575. DOI: 10.1038/nature09535 [PubMed: 21107428]
21. Rad R, et al. A genetic progression model of Braf(V600E)-induced intestinal tumorigenesis reveals targets for therapeutic intervention. Cancer Cell. 2013; 24:15–29. DOI: 10.1016/j.ccr.2013.05.014 [PubMed: 23845441]
22. Rhim AD, et al. EMT and dissemination precede pancreatic tumor formation. Cell. 2012; 148:349–361. DOI: 10.1016/j.cell.2011.11.025 [PubMed: 22265420]
23. Stathis A, Moore MJ. Advanced pancreatic carcinoma: current treatment and future challenges. Nat Rev Clin Oncol. 2010; 7:163–172. DOI: 10.1038/nrclinonc.2009.236 [PubMed: 20101258]
24. Yachida S, et al. Distant metastasis occurs late during the genetic evolution of pancreatic cancer. Nature. 2010; 467:1114–1117. DOI: 10.1038/nature09515 [PubMed: 20981102]
25. Schneider G, et al. IKKalpha controls p52/RelB at the skp2 gene promoter to regulate G1- to S-phase progression. EMBO J. 2006; 25:3801–3812. DOI: 10.1038/sj.emboj.7601259 [PubMed: 16902410]
26. Hamidi T, et al. Nuclear protein 1 promotes pancreatic cancer development and protects cells from stress by inhibiting apoptosis. J Clin Invest. 2012; 122:2092–2103. DOI: 10.1172/JCI60144 [PubMed: 22565310]

27. Redston MS, et al. p53 mutations in pancreatic carcinoma and evidence of common involvement of homocopolymer tracts in DNA microdeletions. Cancer Res. 1994; 54:3025–3033. [PubMed: 8187092]
28. Collisson EA, et al. Subtypes of pancreatic ductal adenocarcinoma and their differing responses to therapy. Nat Med. 2011; 17:500–503. DOI: 10.1038/nm.2344 [PubMed: 21460848]
29. Moffitt RA, et al. Virtual microdissection identifies distinct tumor- and stroma-specific subtypes of pancreatic ductal adenocarcinoma. Nat Genet. 2015; 47:1168–1178. DOI: 10.1038/ng.3398 [PubMed: 26343385]
30. Maresch R, et al. Multiplexed pancreatic genome engineering and cancer induction by transfection-based CRISPR/Cas9 delivery in mice. Nat Commun. 2016; 7:10770.doi: 10.1038/ncomms10770 [PubMed: 26916719]
31. Morohoshi T, Held G, Kloppel G. Exocrine pancreatic tumours and their histological classification. A study based on 167 autopsy and 97 surgical cases. Histopathology. 1983; 7:645–661. [PubMed: 6313514]
32. Iacobuzio-Donahue CA, et al. DPC4 gene status of the primary carcinoma correlates with patterns of failure in patients with pancreatic cancer. J Clin Oncol. 2009; 27:1806–1813. DOI: 10.1200/JCO.2008.17.7188 [PubMed: 19273710]
33. Winter JM, et al. Absence of E-cadherin expression distinguishes noncohesive from cohesive pancreatic cancer. Clin Cancer Res. 2008; 14:412–418. DOI: 10.1158/1078-0432.CCR-07-0487 [PubMed: 18223216]
34. Hruban RH, et al. Pathology of genetically engineered mouse models of pancreatic exocrine cancer: consensus report and recommendations. Cancer Res. 2006; 66:95–106. DOI: 10.1158/0008-5472.CAN-05-2168 [PubMed: 16397221]
35. Hingorani SR, et al. Preinvasive and invasive ductal pancreatic cancer and its early detection in the mouse. Cancer Cell. 2003; 4:437–450. [PubMed: 14706336]
36. Nakhai H, et al. Ptf1a is essential for the differentiation of GABAergic and glycinergic amacrine cells and horizontal cells in the mouse retina. Development. 2007; 134:1151–1160. DOI: 10.1242/dev.02781 [PubMed: 17301087]
37. Aguirre AJ, et al. Activated Kras and Ink4a/Arf deficiency cooperate to produce metastatic pancreatic ductal adenocarcinoma. Genes Dev. 2003; 17:3112–3126. DOI: 10.1101/gad.1158703 [PubMed: 14681207]
38. Jonkers J, et al. Synergistic tumor suppressor activity of BRCA2 and p53 in a conditional mouse model for breast cancer. Nat Genet. 2001; 29:418–425. DOI: 10.1038/ng747 [PubMed: 11694875]
39. Lee CL, et al. Generation of primary tumors with Flp recombinase in FRT-flanked p53 mice. Dis Model Mech. 2012; 5:397–402. DOI: 10.1242/dmm.009084 [PubMed: 22228755]
40. Chytil A, Magnuson MA, Wright CV, Moses HL. Conditional inactivation of the TGF-beta type II receptor using Cre:Lox. Genesis. 2002; 32:73–75. [PubMed: 11857781]
41. Bronner IF, Quail MA, Turner DJ, Swerdlow H. Improved Protocols for Illumina Sequencing. Curr Protoc Hum Genet. 2014; 80 18 12 11-42. doi: 10.1002/0471142905.hg1802s80
42. Stephens PJ, et al. Massive genomic rearrangement acquired in a single catastrophic event during cancer development. Cell. 2011; 144:27–40. DOI: 10.1016/j.cell.2010.11.055 [PubMed: 21215367]
43. Jentsch I, Adler ID, Carter NP, Speicher MR. Karyotyping mouse chromosomes by multiplex-FISH (M-FISH). Chromosome Res. 2001; 9:211–214. [PubMed: 11330395]
44. Keane TM, et al. Mouse genomic variation and its effect on phenotypes and gene regulation. Nature. 2011; 477:289–294. DOI: 10.1038/nature10413 [PubMed: 21921910]
45. Ye K, Schulz MH, Long Q, Apweiler R, Ning Z. Pindel: a pattern growth approach to detect break points of large deletions and medium sized insertions from paired-end short reads. Bioinformatics. 2009; 25:2865–2871. DOI: 10.1093/bioinformatics/btp394 [PubMed: 19561018]
46. Barretina J, et al. The Cancer Cell Line Encyclopedia enables predictive modelling of anticancer drug sensitivity. Nature. 2012; 483:603–607. DOI: 10.1038/nature11003 [PubMed: 22460905]
47. Alexandrov LB, et al. Signatures of mutational processes in human cancer. Nature. 2013; 500:415–421. DOI: 10.1038/nature12477 [PubMed: 23945592]

48. Parekh S, Ziegenhain C, Vieth B, Enard W, Hellmann I. The impact of amplification on differential expression analyses by RNA-seq. Sci Rep. 2016; 6:25533.doi: 10.1038/srep25533 [PubMed: 27156886]
49. Macosko EZ, et al. Highly Parallel Genome-wide Expression Profiling of Individual Cells Using Nanoliter Droplets. Cell. 2015; 161:1202–1214. DOI: 10.1016/j.cell.2015.05.002 [PubMed: 26000488]
50. Love MI, Huber W, Anders S. Moderated estimation of fold change and dispersion for RNA-seq data with DESeq2. Genome Biol. 2014; 15:550.doi: 10.1186/s13059-014-0550-8 [PubMed: 25516281]
51. Huang da W, Sherman BT, Lempicki RA. Systematic and integrative analysis of large gene lists using DAVID bioinformatics resources. Nat Protoc. 2009; 4:44–57. DOI: 10.1038/nprot.2008.211 [PubMed: 19131956]
52. Subramanian A, et al. Gene set enrichment analysis: a knowledge-based approach for interpreting genome-wide expression profiles. Proc Natl Acad Sci U S A. 2005; 102:15545–15550. DOI: 10.1073/pnas.0506580102 [PubMed: 16199517]
53. Schaefer CF, et al. PID: the Pathway Interaction Database. Nucleic Acids Res. 2009; 37:D674–679. DOI: 10.1093/nar/gkn653 [PubMed: 18832364]
54. Du P, Kibbe WA, Lin SM. lumi: a pipeline for processing Illumina microarray. Bioinformatics. 2008; 24:1547–1548. DOI: 10.1093/bioinformatics/btn224 [PubMed: 18467348]
55. Ritchie ME, et al. limma powers differential expression analyses for RNA-sequencing and microarray studies. Nucleic Acids Res. 2015; 43:e47.doi: 10.1093/nar/gkv007 [PubMed: 25605792]
56. Friedrich MJ, et al. Genome-wide transposon screening and quantitative insertion site sequencing for cancer gene discovery in mice. Nat Protoc. 2017; 12:289–309. DOI: 10.1038/nprot.2016.164 [PubMed: 28079877]
57. Meerbrey KL, et al. The pINDUCER lentiviral toolkit for inducible RNA interference in vitro and in vivo. Proc Natl Acad Sci U S A. 2011; 108:3665–3670. DOI: 10.1073/pnas.1019736108 [PubMed: 21307310]
58. Kutner RH, Zhang XY, Reiser J. Production, concentration and titration of pseudotyped HIV-1-based lentiviral vectors. Nat Protoc. 2009; 4:495–505. DOI: 10.1038/nprot.2009.22 [PubMed: 19300443]
59. Weber J, et al. CRISPR/Cas9 somatic multiplex-mutagenesis for high-throughput functional cancer genomics in mice. Proc Natl Acad Sci U S A. 2015; 112:13982–13987. DOI: 10.1073/pnas.1512392112 [PubMed: 26508638]
60. Cerami E, et al. The cBio cancer genomics portal: an open platform for exploring multidimensional cancer genomics data. Cancer Discov. 2012; 2:401–404. DOI: 10.1158/2159-8290.CD-12-0095 [PubMed: 22588877]
61. Gao J, et al. Integrative analysis of complex cancer genomics and clinical profiles using the cBioPortal. Sci Signal. 2013; 6:l1.doi: 10.1126/scisignal.2004088
62. Uhlen M, et al. Proteomics. Tissue-based map of the human proteome. Science. 2015; 347:1260419.doi: 10.1126/science.1260419 [PubMed: 25613900]
63. Hoadley KA, et al. Multiplatform analysis of 12 cancer types reveals molecular classification within and across tissues of origin. Cell. 2014; 158:929–944. DOI: 10.1016/j.cell.2014.06.049 [PubMed: 25109877]

Europe PMC Funders Author Manuscripts

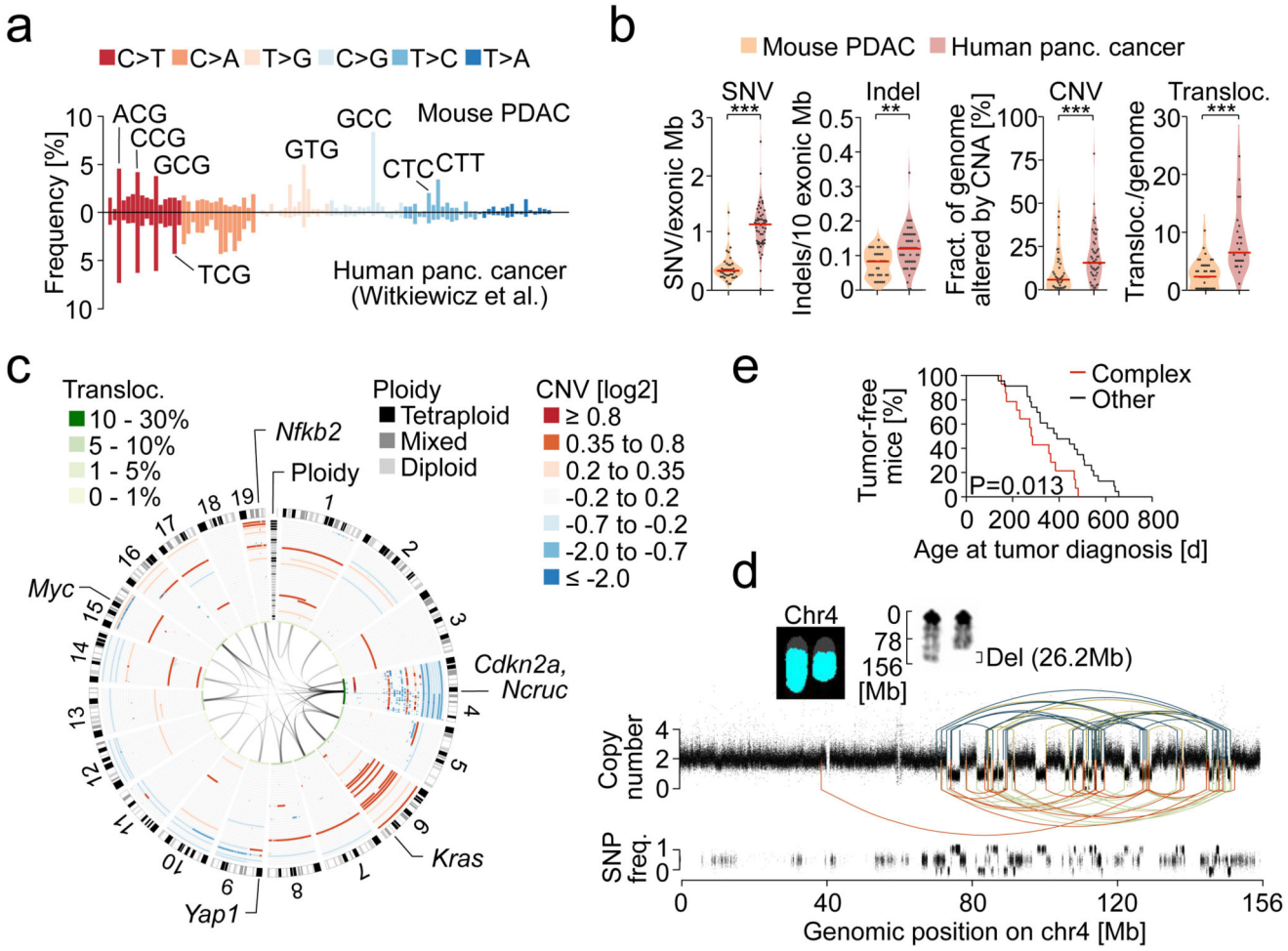

Figure 1. Genetic landscape of mouse PDAC and comparison to the human disease.

a, Trinucleotide context-dependent SNV frequencies in mouse (n=38 PK mice) and human PDAC (n=51 patients from6) derived from WES. **b**, SNV, indel, CNA and translocation burdens by WES, aCGH and M-FISH in PK mice (n=38) and human PDAC (n=51 patients for SNV, indel, CNA [data from6] and n=24 cell lines for translocations). **P=0.002, ***P≤0.001, two-sided Mann-Whitney test; bars, median. **c**, CNAs, ploidy and translocations in PK mice (n=38), detected by aCGH and M-FISH. Mixed ploidy, n≥3 diploid/tetraploid cells in 10 karyotypes. **d**, Rearrangement graph showing chr4 chromothripsis in mPDAC S821, based on WGS. Haplotype-specific chromosome content loss confirmed by M-FISH (n=10/10 karyotypes). **e**, Age at tumor diagnosis of mice having cancers with (n=14) or without (n=23) complex/clustered chromosomal rearrangements (n≥10 CNAs/chromosome). Two-sided log-rank test.

Europe PMC Funders Author Manuscripts

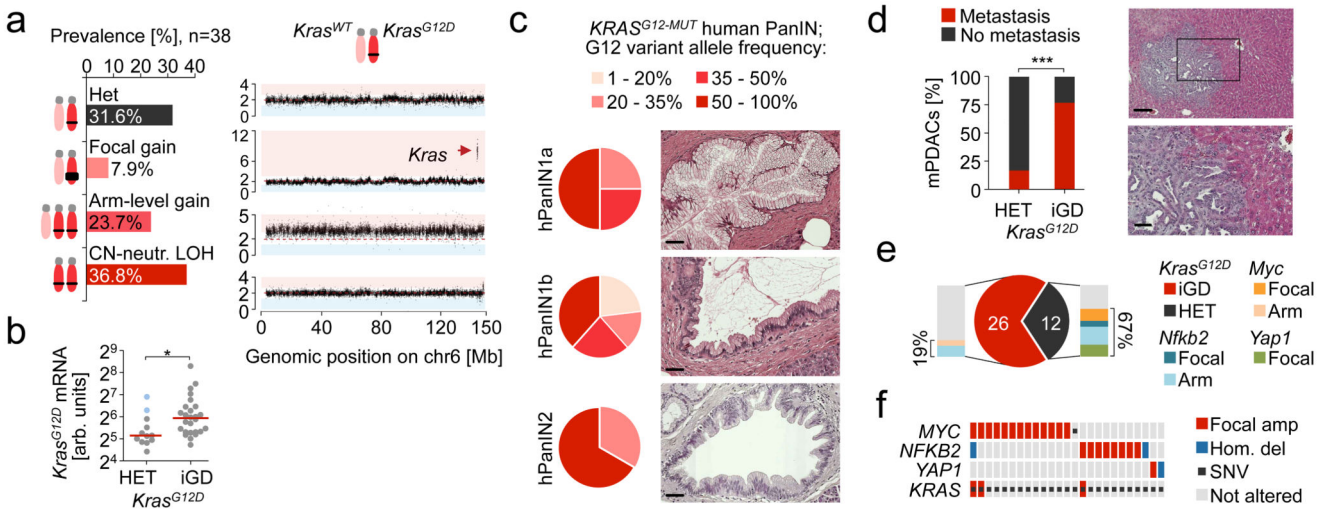

Figure 2. Mutant *KRAS* gene dosage increase occurs early in PDAC evolution and drives metastasis.

a, *Kras*^{G12D} gene dosage "states" defined by aCGH, WES and M-FISH (n=38 PK mice). Exemplary CNV-plot for each "state" on the right, y-axis, copy number **b**, Allele-specific *Kras*^{G12D} mRNA expression in *Kras*$^{G12D\text{-}iGD}$ (n=26 mice) and *Kras*$^{G12D\text{-}HET}$ mPDACs (n=12 mice) by combined amplicon-based RNA-Seq and qRT-PCR. *P=0.02, two-sided Mann-Whitney test; bars, median. **c**, Codon-12 variant allele frequency of microdissected *KRAS*^{G12} mutant hPanIN (n=20) by amplicon-based deep sequencing. H&E stains show histopathologic stages of microdissected hPanINs. Scale bars, 50 μm. **d**, Macro-/micro-metastasis prevalence in *Kras*$^{G12D\text{-}HET}$ (n=12) vs. *Kras*$^{G12D\text{-}iGD}$ (n=26) mPDACs. (***P=0.001, two-sided Fisher's exact test). Liver metastasis, H&E. Scale bars, 150 μm (top) and 50 μm (bottom); square, zoom-in area. **e**, *Kras*$^{G12D\text{-}HET}$ mPDAC amplify alternative oncogenes (*Myc*, *Nfkb2* or *Yap1*) to intensify partial aspects of Ras downstream signaling. Focal, focal amplification; Arm, arm-level amplification. **f**, Amplification of *MYC*, *NFKB2* or *YAP1* in *KRAS*^{MUT} human PDAC. Note, these amplified genes can not only collaborate with *KRAS*$^{MUT\text{-}Het}$ but also with *KRAS*$^{MUT\text{-}iGD}$. Data from6.

Europe PMC Funders Author Manuscripts

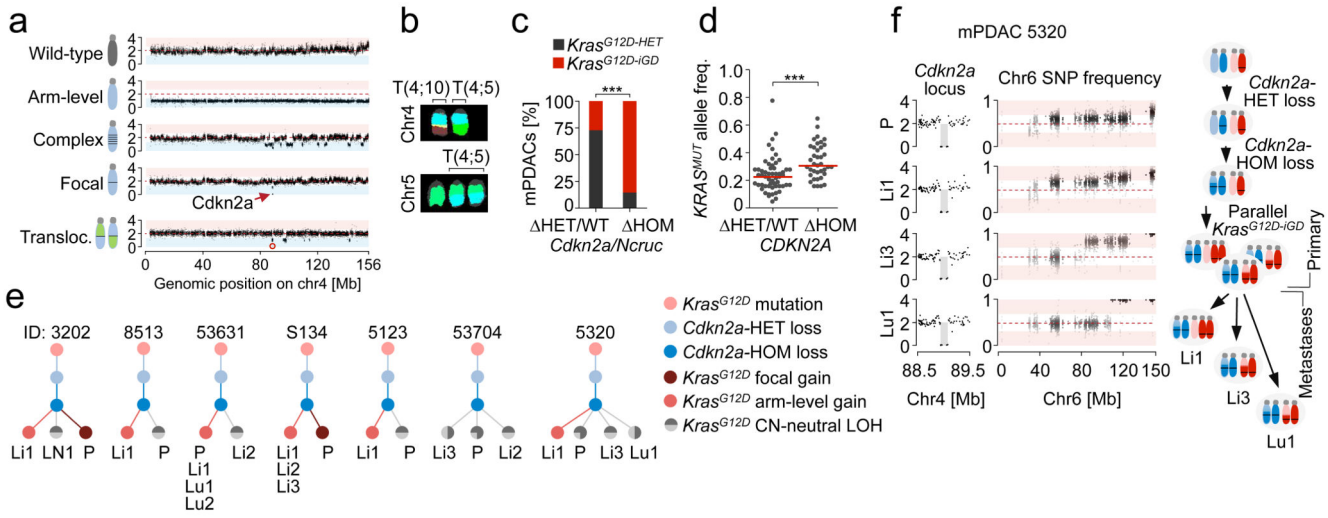

Figure 3. *Cdkn2a* alteration "states" dictate distinct evolutionary PDAC trajectories.

a, Chr4 alteration types involving *Cdkn2a* by aCGH/M-FISH (n=38 PK mice). Complex rearrangements, n≥10 CNAs/chromosome. Examplary CNV plots on the right; y-axis, copy number. **b**, Translocations affecting chr4/*Cdkn2a* in mPDAC-R1035 by M-FISH (10/10 karyotypes). **c**, Prevalence of $Kras^{G12D\text{-}iGD}$ in mPDAC with homozygously (ΔHOM, n=27) vs. wild-type/heterozygously (ΔHET/WT, n=11) deleted *Cdkn2a/Ncruc*. ***P=0.001, two-sided Fisher's exact test, OR 15.3, 95% CI 2.8-83.9. **d**, *KRAS* variant allele frequencies in human PDAC with wild-type/heterozygously (n=56) vs. homozygously deleted (n=38) *CDKN2A*. Data from6. ***P≤0.001, two-sided Mann-Whitney test; bars, median. **e**, Sequential order of *Cdkn2a* and $Kras^{G12D}$ alterations. Chr4 and chr6 CNA/LOH patterns (based on aCGH,WES) of primary mPDACs (n=13 PK mice) and associated metastases (n=25). For seven mPDACs and 16 associated metastases the order of genetic events (dots) could be reconstructed. Bifurcations, divergent evolution of clones; lines, lengths do not represent evolutionary distances; P, primary tumor; Li/Lu/LN, liver/lung/lymph node metastasis. **f**, Detailed chr4/chr6 CNV/LOH profiles for mPDAC5320 primary/metastases. *Cdkn2a* deletions are identical in all lesions (y-axis, copy number). SNP frequency analysis by WES shows distinct chr6 SNP patterns in metastases and a composite picture in the primary, showing convergent evolution of different $Kras^{G12D\text{-}iGD}$-gains upon $Cdkn2a^{\Delta HOM}$. Scheme, combined interpretation of WES/aCGH data.

Europe PMC Funders Author Manuscripts

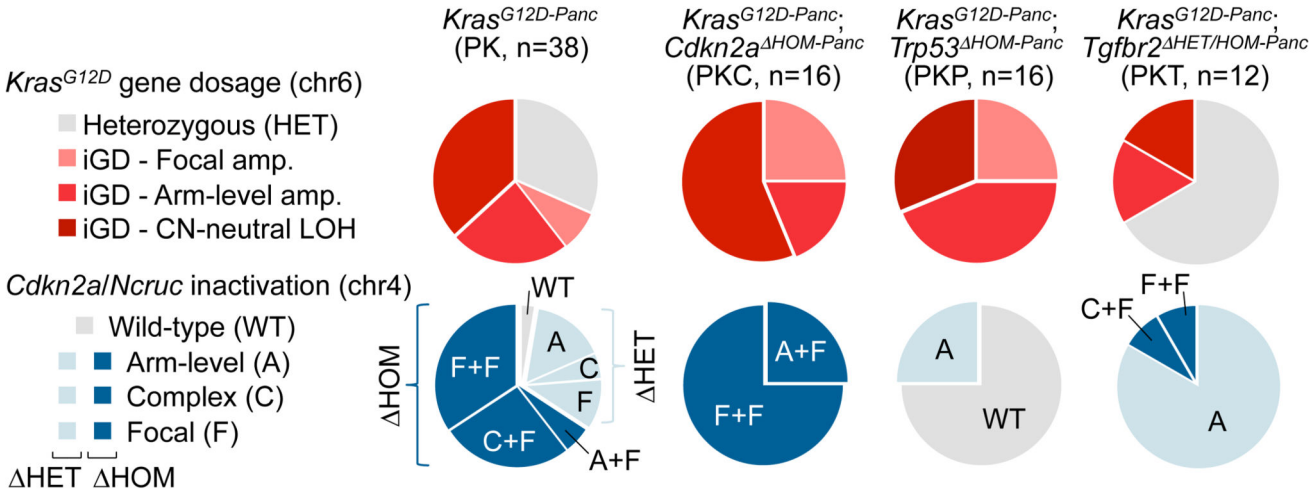

Figure 4. Defined allelic states and/or combinations of hallmark PDAC tumor-suppressor alterations license oncogenic dosage variation.

Types and frequencies of *Kras*^{G12D} gene dosage gains and *Cdkn2a* inactivations, defined by aCGH and amplicon-based *Kras*^{G12D} sequencing in PDAC mouse models expressing pancreas-specific *Kras*^{G12D} alone (PK) or in combination with engineered *Cdkn2a*$^{\Delta HOM}$ (PKC), *Trp53*$^{\Delta HOM}$ (PKP) or *Tgfbr2*$^{\Delta HET/HOM}$ (PKT) inactivation.

Europe PMC Funders Author Manuscripts

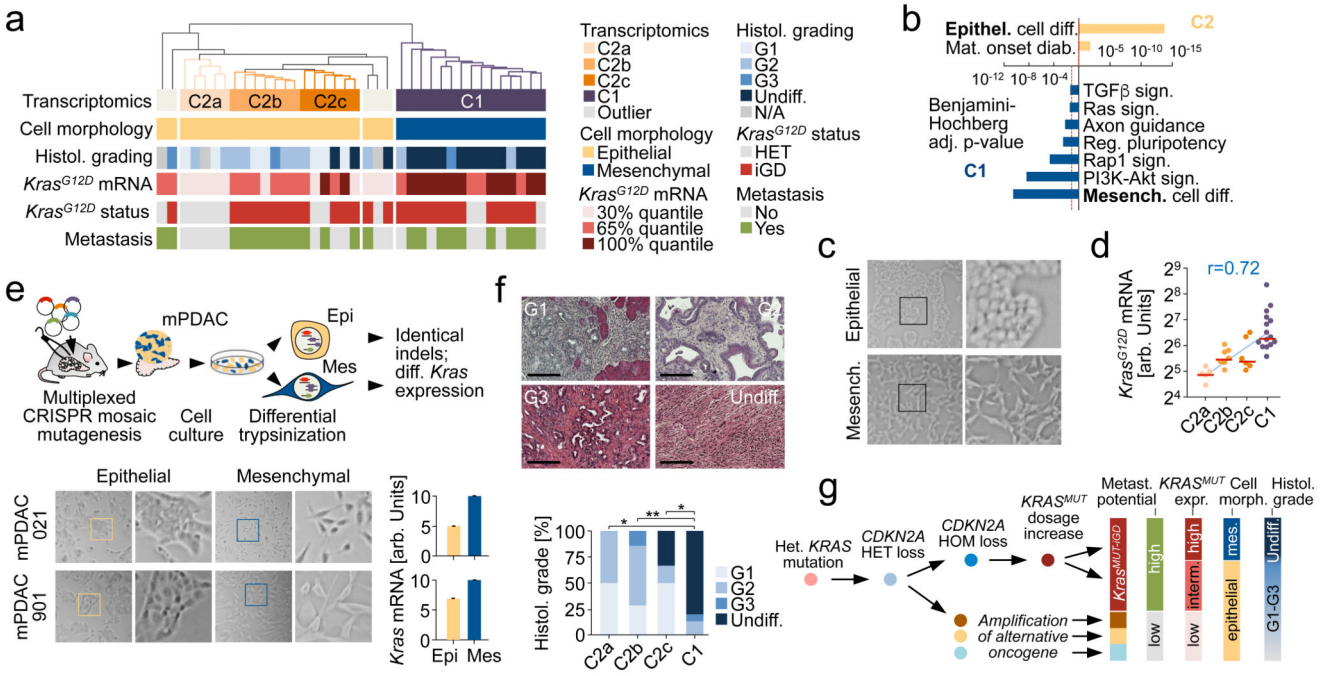

Figure 5. Integrative analyses of PDAC genomics, transcriptomics, cellular phenotypes and histopathologies link molecular, morphologic and clinical disease characteristics.

a, Unbiased hierarchical clustering of primary mPDAC culture transcriptomes (PK mice). Cell morphology, histopathological grading, *Kras*^{G12D} mRNA expression, genetic *Kras*^{G12D} status and presence/absence of metastasis integrated below. **b**, Selected gene sets from gene-set enrichment analysis of clusters C2 vs. C1. (full list in Supplementary Table 13,14). **c**, mPDAC cultures with mesenchymal/epithelial morphology from clusters C1/C2, respectively. 100x magnification; squares, zoom-in area. **d**, *Kras*^{G12D}-allele-specific mRNA levels in mPDAC transcriptional clusters, combined amplicon-based RNA-Seq and qRT-PCR (C2a/b/c/C1, n=5/7/6/15 mice). P=1.9*10^{-6}, two-sided Pearson correlation; bars, median. **e**, CRISPR/Cas9-mediated multiplexed somatic inactivation of PDAC-relevant tumor suppressors by electroporation-based transfection to achieve low-frequency mosaicism and clonal tumor outgrowth. Differential trypsinization separates epithelial/mesenchymal cells in mPDACs with mixed morphologies (100x magnification; squares, zoom-in area). CRISPR/Cas9-induced indel signatures are identical in epithelial/mesenchymal pairs (Extended data Fig. 8), indicating common cell of origin. Total *Kras* mRNA levels in epithelial/mesenchymal pairs (qRT-PCR, normalized to *Gapdh*, n=2 technical replicates). Bars, mean; error bars, SEM. **f**, mPDAC histophathological grading in transcriptional clusters (C2a/b/c/C1, n=4/7/6/15, single section per mPDAC). Representative sections (H&E) shown. *Benjamini-Hochberg-adj. P≤0.05, **P=0.005; two-sided Fisher's exact test; scale bars, 150μm. **g**, Simplified model of PDAC evolution reconciling molecular, morphologic and clinical disease characteristics. *KRAS*$^{G12D\text{-}iGD}$ gain or alternative oncogenic amplifications *(Myc/Yap1/Nfkb2)* are critical for early disease progression. Different oncogenic gains and dosages evolve along distinct evolutionary routes, licensed by defined allelic states (heterozygous/homozygous) and/or combinations of hallmark tumor-suppressor alterations. For simplicity, only the prototype tumor suppressor gene *CDKN2A* is

Europe PMC Funders Author Manuscripts

shown. Not visualized: *TP53*$^{\Delta HOM}$ loss, also promoting *KRAS*$^{MUT\text{-}iGD}$, or *TGFBR2*$^{\Delta HET/HOM}$ inactivation, supporting evolution through *CDKN2A*^{HET}/*KRAS*$^{MUT\text{-}HET}$ trajectories. Depicted alternative trajectories are typical, but not completely exclusive, e.g. *MYC* or *NFKB2* amplifications, which drive *KRAS*$^{MUT\text{-}HET}$ cancers, can also cooperate with *KRAS*$^{MUT\text{-}iGD}$. Major aspects of a cancer´s biology/phenotype are linked to differential evolution.

Europe PMC Funders Author Manuscripts